

Using pyrite composition to track the multi-stage fluids superimposed on a porphyry Cu system

CHAO WU^{1,2,3,4}, DAVID R. COOKE^{3,4,†}, MICHAEL J. BAKER^{3,4}, LEJUN ZHANG^{3,4,‡}, PEI LIANG⁶,
JING FANG¹, PAUL OLIN⁴, LEONID V. DANYUSHEVSKY⁷, AND HUAYONG CHEN^{1,2,5,*}

¹Key Laboratory of Mineralogy and Metallogeny, Guangzhou Institute of Geochemistry, Chinese Academy of Sciences, Guangzhou 510640, China

²CAS Center for Excellence in Deep Earth Science, Guangzhou, 510640, China

³ARC Research Hub for Transforming the Mining Value Chain, TMVC, University of Tasmania, Private Bag 79, Hobart, Tasmania 7001, Australia

⁴CODES, Centre for Ore Deposit and Earth Sciences, University of Tasmania, Hobart, Tasmania 7001, Australia

⁵University of Chinese Academy of Sciences, Beijing 100049, China

⁶Civil and Resource Engineering School, University of Science & Technology Beijing, Beijing 100083, China

⁷Hobart, Tasmania, Australia

ABSTRACT

The Yulekenhalasu porphyry Cu-Mo deposit (0.2 Mt Cu at 1.04 wt% and 0.012 Mt Mo at 0.06 wt%) is located in the Devonian Halasu copper belt, East Junggar block, northwest China. At Yulekenhalasu, Cu and Mo mineralization commonly occurs as disseminated sulfides or veinlets in porphyry-related alteration zones. Five alteration stages have been identified, including porphyry-type alteration, i.e., sodic-calcic (stage I), potassic (stage IIa), propylitic (stage IIb), and phyllic (stage III) alteration, and widespread late Cu sulfide-bearing veins (stage IV) cross-cutting porphyry-type alteration, plus a post-ore fault-controlled argillic alteration (stage V). Stages IV and V have overprinted porphyry-type alteration (stages I–III).

Anomalous concentrations of trace elements in stage IIb pyrite (e.g., Ti, Zr, Gd, and Hf) are due to the presence of micro-inclusions (e.g., zircon and rutile) in the low-temperature (~200 °C) propylitic zone. Cu, Ag, Co, and Mn, occurring as stoichiometric substitutions or as tetrahedrite inclusions in overprinting stage IV pyrite, were sourced directly from the primary hydrothermal fluid. The enrichment of distal pathfinder elements (e.g., Cr, Au, and Tl) in overprinting stage V pyrite was caused by a low-temperature (~160 °C) hydrothermal event related to regional orogenic Au mineralization. The spatial variation of Se/S in pyrite among various paragenetic stages were influenced by changes in the hydrothermal fluid composition and temperature, with the latter having the effect of decreasing pyrite Se/S. Lower Se concentrations in pyrite of stages IIb and III close to the orebody are explained by relatively higher temperatures in the locus of mineralization. This may provide a potential vectoring tool to mineralization using pyrite geochemistry in porphyry deposits.

Systematic thermodynamic calibrations were applied to pyrite compositions to fingerprint the corresponding Se/S and Co/Ni ratios of fluids and further to develop a complete metallogenic model for Yulekenhalasu. The Devonian diorite porphyry generated fluids that produced the early porphyry-type alteration. High Co/Fe (average $\sim 1 \times 10^{-4}$) and Ni/Fe (average $\sim 3 \times 10^{-6}$) ratios of fluid for late Cu sulfide-bearing veins, combined with higher Se/S (average $\sim 6 \times 10^{-7}$) than orogenic Au deposits (average $\sim 3 \times 10^{-8}$), indicate that the fluids possibly derived from a Late Devonian-Carboniferous mafic intrusion. Argillic alteration assemblages forming at ca. 280 Ma host pyrite relatively enriched in Au (average 0.1 ppm, with native gold inclusions). Therefore it is likely related to a regional orogenic gold mineralizing event in the Early Permian that overprinted Devonian mineralization. Although spatially contiguous, hydrothermal alteration and hypogene mineralizing stages identified herein represent discrete episodes of hydrothermal activities at Yulekenhalasu. The multi-stage alteration features observed at Yulekenhalasu may provide insights into the complete evolutionary history of Paleozoic porphyry Cu deposit systems in the Central Asian orogenic belt. This study contributes to a better understanding of the metallogenic and exploration models of porphyry Cu deposits overprinted by multi-stage hydrothermal events, which is economically important in Phanerozoic orogenic belts.

Keywords: Central Asian Orogenic Belt, Yulekenhalasu, porphyry Cu-Mo deposit, pyrite composition, superimposed alteration and mineralization

INTRODUCTION

The Central Asian Orogenic Belt is one of the world's largest subduction-accretionary orogens (Carroll et al. 1990; Jahn 2004; Jahn et al. 2000; Mossakovsky et al. 1994; Şengör et al. 1993;

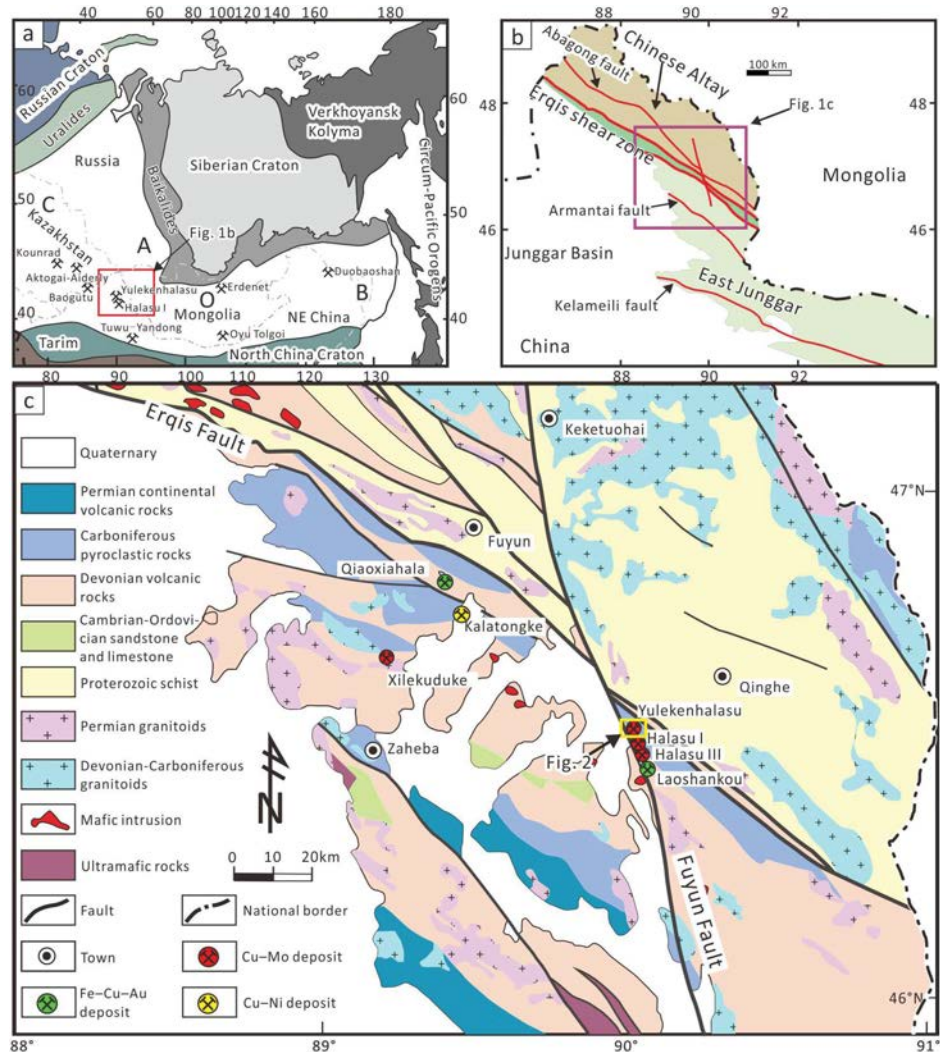
Xiao et al. 2009b; Fig. 1a). It hosts several giant porphyry Cu deposits, including Oyu Tolgoi, Erdenet, and Aktogai-Aiderly, and is one of the most important porphyry Cu belts in the world in terms of proven resources (Mao et al. 2014; Perelló et al. 2001; Seltmann et al. 2014; Yakubchuk 2004; Yakubchuk et al. 2012). Most of the porphyry deposits in the Central Asian Orogenic Belt formed in island- or continental-arc settings but were subject to Late Paleozoic collision and subsequent post-collisional and

* Corresponding author E-mail: huayongchen@gig.ac.cn

† Orcid 0000-0003-3096-5658

‡ Orcid 0000-0003-0874-8526

FIGURE 1. (a) Regional tectonic map of the Central Asian Orogenic Belt (modified from Jahn et al. 2000). (b) Tectonic map of the Chinese Altay–East Junggar terrane (modified from Wan et al. 2014). (c) Geologic map of the southeastern Chinese Altay orogenic belt and northeastern Junggar block, NW China (modified from Zhang et al. 2009). (Color online.)



intra-plate extension, e.g., Tuwu-Yandong (Wang et al. 2019; Xiao et al. 2017), Yuhai (Wang et al. 2018), and Sanchakou Cu deposits (Qin et al. 2009; Wang et al. 2022), creating challenges and opportunities for mineral exploration (Heinhorst et al. 2000; Nie et al. 2004; Yakubchuk 2004; Zhao et al. 1997). The Yulekenhalasu deposit, with a metal tonnage greater than 0.2 Mt Cu and an average grade at 1.04% Cu (Xiang 2013), is one of the earliest discovered porphyry Cu deposits in the Chinese Altay–East Junggar orogenic belt (Fig. 1). Previous studies of the deposit have focused on magmatism (Wu et al. 2015; Yang et al. 2014), quartz-hosted fluid inclusions (Geng et al. 2013; Yang et al. 2012), and trace element variations in sulfides (Hong et al. 2021b; Hong et al. 2018). These studies suggest that the Devonian Yulekenhalasu system is characterized by typical porphyry-type mineralization and alteration but was overprinted by late-stage hydrothermal events (Hong et al. 2021b; Liu et al. 1991; Wu et al. 2015; Xue et al. 2016; Yan et al. 2006; Yang et al. 2014). However, previous studies lumped multiple alteration stages into porphyry-type and overprinting categories, which lack detailed descriptions, and models for their origins and conditions of formation during multi-stage hydrothermal events in different

tectonic settings are poorly understood.

To describe the detailed paragenetic history of Yulekenhalasu, we present new geological observations and geochemical data obtained from LA-ICP-MS analyses of hydrothermal pyrite sampled from a selection of alteration zones across the deposit. These new data are used to constrain the complex hydrothermal evolution of Yulekenhalasu. Furthermore, a new metallogenic model for porphyry deposits that preserve the overprint of multi-stage hydrothermal events, which are ubiquitous in the Central Asian Orogenic Belt, is developed to guide the exploration of porphyry Cu deposits in orogenic belts with prolonged evolutionary histories.

REGIONAL GEOLOGICAL SETTING

The Yulekenhalasu porphyry Cu deposit is located on the northern margin of the East Junggar belt. It is part of the Halasu copper belt, which contains, from north to south, the Yulekenhalasu, Dunke'erman, and Halasu I, II, and III copper deposits (Fig. 1). Halasu I (0.17 Mt Cu with an average grade of 0.34% Cu) and Yulekenhalasu are the two largest deposits in the belt (Xiang 2013; Yang et al. 2014).

Four distinct metallogenic belts were recognized in the Chinese Altay–East Junggar region by Wan et al. (2017) and Yang et al. (2018a), including a volcanogenic massive sulfide (VMS) Cu–Pb–Zn belt and a rare metal pegmatite belt in the Chinese Altay, a shear zone-hosted Au (or orogenic Au) belt along the Erqis fault, and a porphyry Cu–Mo±Au belt in East Junggar (Fig. 1c). The VMS deposits (e.g., Ashele Cu–Zn deposit) formed in the Lower to Middle Devonian extensional arc-related submarine basins, and shear zone-hosted Au deposits (e.g., Kekesayi and Kubusu Au deposits) formed at the Early Permian transpressional terrane boundaries (Niu et al. 2020; Wan et al. 2014; Yang et al. 2018a, 2018b). The East Junggar porphyry deposits formed in three periods at convergent continental margins: ca. 408 Ma (e.g., Hersai; Du et al. 2010), 375 Ma (e.g., Halasu; Yang et al. 2014) and 330 Ma (e.g., Xilekuduke; Long et al. 2011; Wan et al. 2014). East Junggar also hosts the Qiaoxiahala (383.2 ± 4.5 Ma) and Laoshankou (375.2 ± 2.6 Ma) IOCG deposits (Li et al. 2014), and the Kalatongke Cu–Ni magmatic sulfide deposit (287 ± 5 Ma; Han et al. 2004; Fig. 1c).

The Chinese Altay in the northern Chinese Altay–East Junggar zone comprises Middle Ordovician to Late Carboniferous metamorphosed clastic turbidite, limestone, sandstone–shale and island arc-related pyroclastic rocks (Fig. 1) (Xiao et al. 2009b; Yang et al. 2014; Zhang et al. 2009). The Erqis shear zone separates the Chinese Altay from East Junggar (Fig. 1), and contains high-grade gneiss and schist, Paleozoic ophiolitic fragments, and mafic-intermediate lavas (Fig. 1c) (Xue et al. 2016; Yang et al. 2014). Intrusions exposed in the Chinese Altay and Erqis shear zone are divided into two subgroups: Upper Ordovician to Devonian calc-alkaline granitoids (ca. 450–375 Ma) and Carboniferous to Early Permian alkaline granitoids (ca. 340–280 Ma; Wang et al. 2010). The East Junggar terrane contains minor Silurian sedimentary rocks, extensive exposures of Devonian mafic-intermediate volcanic rocks and marine sedimentary rocks, Early to Middle Carboniferous intermediate volcanic- and sedimentary rocks, and Early Permian continental volcanic rocks (Xiao et al. 2009a). In addition to the Devonian to Early Carboniferous calc-alkaline granites and adakites that formed in an island arc setting, East Junggar also contains minor Late Carboniferous and Permian A-type granite dikes, interpreted to have been emplaced in a post-orogenic environment (Fig. 1c) (Wang et al. 2010; Xiao et al. 2009a).

The Erqis shear zone and the Abagong fault are terrane-boundary fault systems within the Chinese Altay–East Junggar (Fig. 1b). Fault systems in East Junggar are mainly NW-trending thrusts (e.g., Armantai and Kelameili faults) and NNW-trending strike-slip faults (Figs. 1b–1c) (e.g., Fuyun fault; Windley et al. 2002). The Fuyun fault (also referred to as the Keketuohai–Ertai fault) is a 180 km long active oblique strike-slip fault that marks the western margin of the Halasu copper belt. It dextrally displaced the Erqis fault by 7 to 8 km (Windley et al. 2002; Fig. 1c), with the Yulekenhalasu deposit sandwiched by the Erqis shear zone to the northwest and Fuyun fault to the west.

DEPOSIT GEOLOGY

Exposed in the area surrounding Yulekenhalasu is a succession of marine volcanic and volcanoclastic rocks consisting principally of the Middle Devonian Beitashan Formation, a sequence of mafic to intermediate lava and tuffs, breccia and sandstone (Hong et al.

2017, 2021a). The Beitashan Formation is unconformably overlain by the Early Carboniferous Jiangbasitao Formation, which consists of, from bottom to top, carbonaceous black shale, siltstone (partially metamorphosed into slate), conglomerate, tuffaceous sandstone, and intermediate tuff intercalated with minor andesite that was deposited in a volcanic arc setting (Zhang et al. 2009). Of the three principal fault orientations recognized in the district [north-northwest (NNW), northeast (NE), and west (W) fault systems; Figs. 1c and 2], the NNW-trending fault system is parallel to the elongated axis of the principal orebodies at Yulekenhalasu and appears closely associated with the regional Fuyun fault which dips steeply to the northeast. West-trending faults are inferred to record sinistral strike-slip movement, whereas the NE-trending faults are tensional faults with sinistral movement (Liu et al. 2010).

Intrusive rocks of Middle Devonian to Carboniferous age include a pre-mineralization porphyritic syenite (ca. 390 Ma), syn-mineralization quartz diorite and diorite porphyry (ca. 382–372 Ma), and post-mineralization quartz granite porphyry and alkali granite porphyry (ca. 350–320 Ma) (Wu et al. 2015; Xiang et al. 2012; Yang et al. 2014). The emplacement of granitoids was generally controlled by the NW-trending fault system, and the intrusions have been cross-cut by W-trending faults (Fig. 2b). The porphyritic syenite occurs as NW-trending stocks and contains coarse-grained K-feldspar as phenocrysts within a groundmass of fine-grained quartz and K-feldspar. The Jiangbasitao Formation is separated from an underlying diorite porphyry by a NW-trending fault (Fig. 2b). The quartz diorite crops out as a large stock along the southern margin of the district, where it intruded the Beitashan Formation (Fig. 2b). It contains plagioclase, quartz, and biotite, with minor alkali feldspar, titanite, apatite, magnetite, and zircon. The diorite porphyry contains phenocrysts of plagioclase, quartz, K-feldspar, minor biotite, and hornblende in a groundmass of plagioclase, quartz, and biotite. Post-mineralization quartz granite porphyry dikes that cut the Jiangbasitao Formation are characterized by quartz and minor plagioclase phenocrysts in a groundmass of quartz, plagioclase, and biotite (Yang et al. 2014). The alkali granite porphyry is dominated by coarse-grained K-feldspar and minor biotite phenocrysts within a groundmass of fine-grained K-feldspar, quartz, and biotite (Wu et al. 2015).

Two mineralized zones (west and east) have been recognized at Yulekenhalasu (Fig. 2b). The eastern zone occurs within the diorite porphyry and hosts the main copper reserve; it is ~800 m long and 20 to 120 m wide (Fig. 2b). The western zone is hosted by basalt and porphyritic syenite in the NW part of the district and is 300 m long and 10–80 m wide. It has been subdivided into three smaller mineralized bodies. Sulfides at Yulekenhalasu include chalcopyrite, pyrite, and molybdenite, with lesser amounts of bornite, galena, sphalerite, and pyrrotite (Fig. 3). Gangue minerals are dominated by quartz, K-feldspar, magnetite, biotite, gypsum, sericite, chlorite, epidote, and calcite (Fig. 3). Ore minerals occur in various textural forms including disseminated grains, veinlets, stockwork veins, replacements, and as cataclases in fault zones.

PARAGENESIS

Five hydrothermal alteration and hypogene mineralizing stages have been identified with stage II consisting of two identifiable alteration assemblages (i.e., IIa and IIb), along with a supergene process at Yulekenhalasu, based on field relationships, including

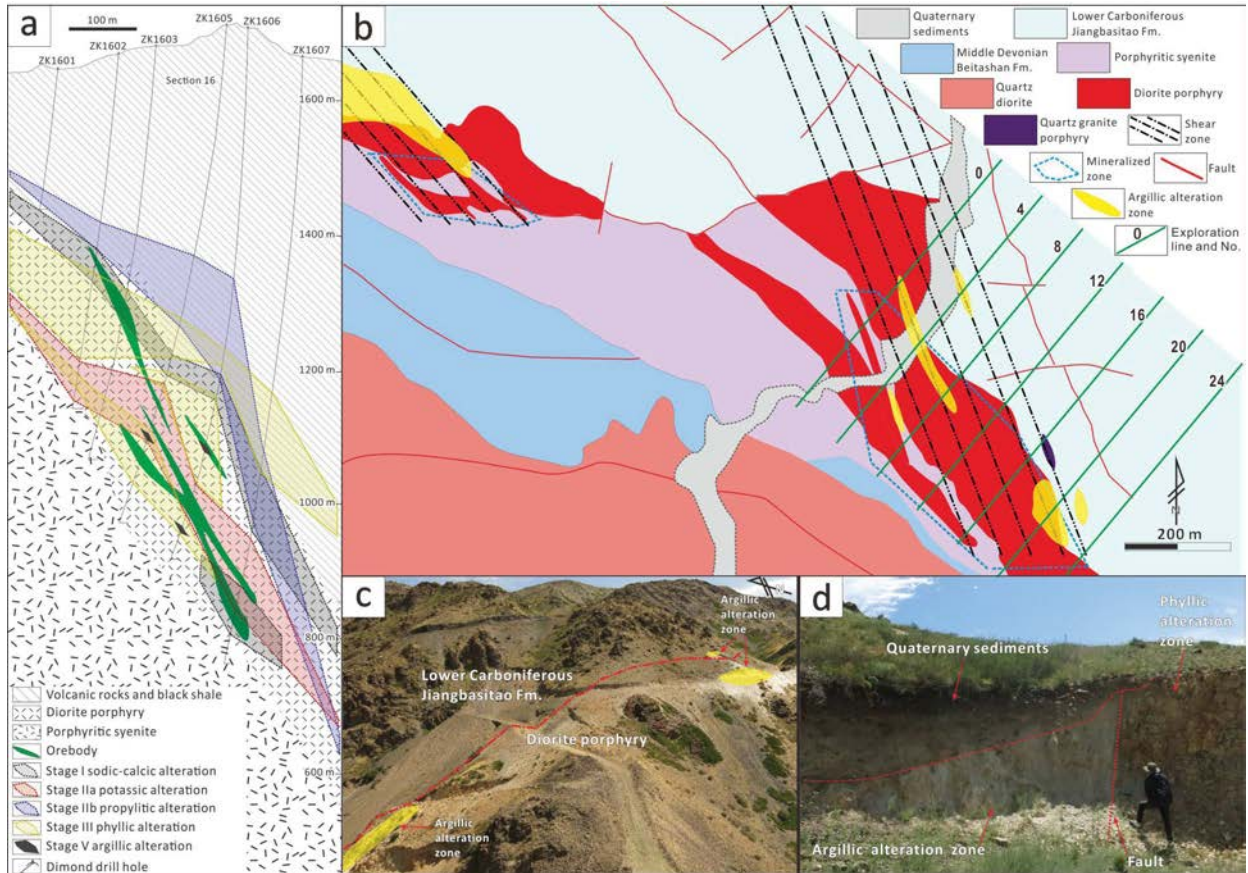
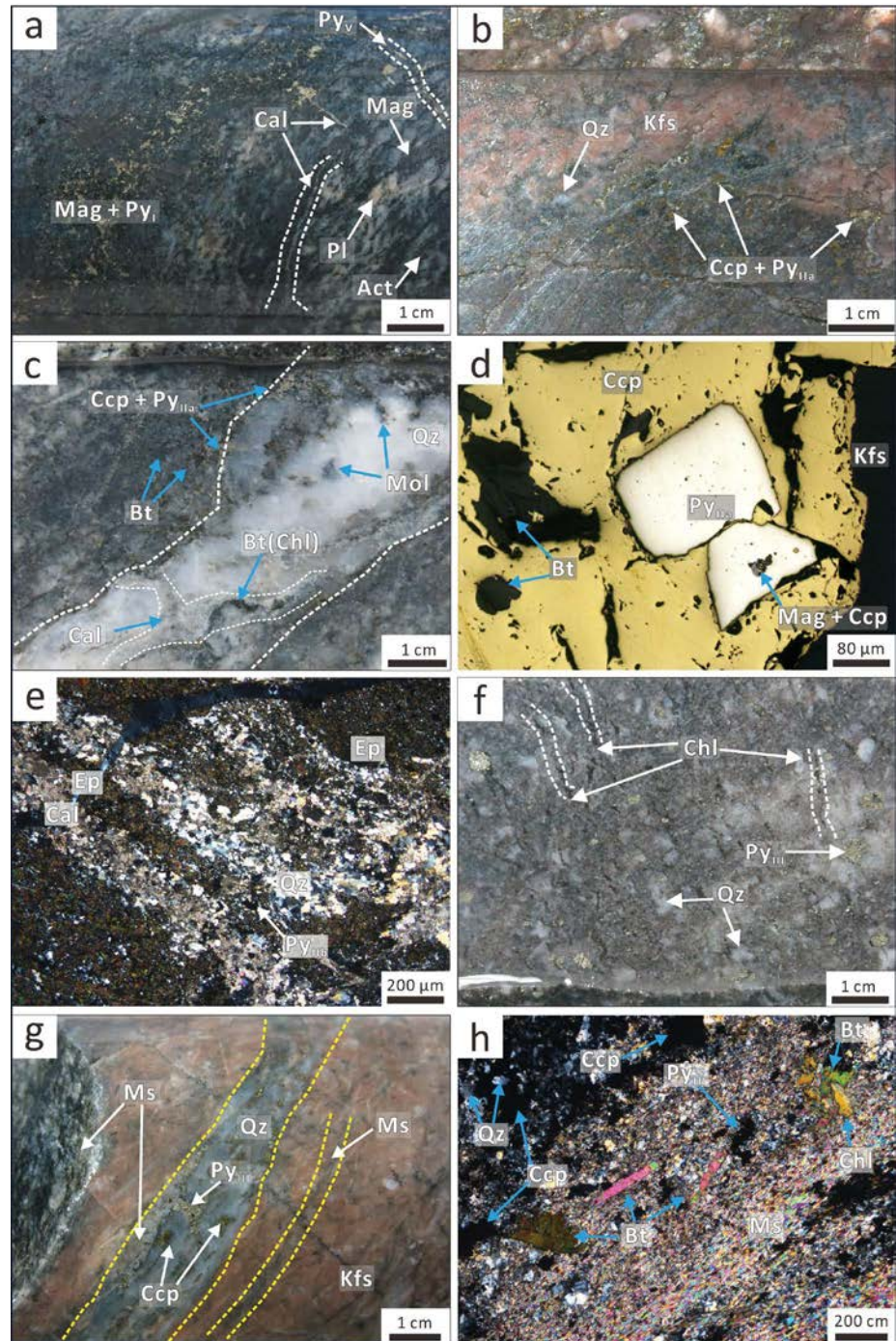


FIGURE 2. (a) Alteration zoning on cross section of exploration line 16 (Wu et al. 2019). (b) Simplified geological map of Yulekenhalasu, showing the spatial distribution of argillic alteration in the eastern and western mineralized zones (Modified from the No. 4 Geological Party of the Xinjiang Bureau of Geology and Mineral Exploration and Development). (c) Photograph of surface-exposed argillic alteration in the eastern mineralized zone. (d) Sharp fault contact between phyllic alteration and argillic alteration. Note that argillic alteration is generally structurally controlled. (Color online.)

Minerals	Stage I: Sodic-calcic alteration	Stage IIa: Potassic alteration	Stage IIb: Propylitic alteration	Stage III: Phyllic alteration	Stage IV: Cu sulfide-bearing veins	Stage V: Argillic alteration	Supergene alteration
Plagioclase	Abundant						
Actinolite							
Quartz	Trace						
K-feldspar		Abundant					
Biotite		Abundant					
Magnetite					Abundant		
Pyrite					Abundant		
Chalcopyrite					Abundant		
Molybdenite					Abundant		
Anhydrite		Abundant					Local
Titanite		Trace					
Apatite		Trace					
Calcite			Abundant				
Epidote	Trace		Abundant				
Chlorite			Abundant				
Muscovite			Abundant				
Illite						Abundant	
Bornite		Trace			Abundant		
Sphalerite					Abundant		
Galena					Abundant		
Montmorillonite						Abundant	
Hematite		Trace					Local
Malachite							Local
Jarosite							Local
Azurite							Local

FIGURE 3. Mineral paragenesis for the Yulekenhalasu copper deposit.

FIGURE 4. Representative photographs and photomicrographs of alteration and mineralization assemblages from Yulekenhalasu. **(a)** Stage I sodic-calcic alteration with randomly oriented magnetite and actinolite replacing igneous biotite (46°36'17.01" N, 90°1'50.90" E; drill hole ZK2005, 890 m depth). **(b)** Stage IIa potassic alteration characterized by fine-grained K-feldspar and quartz altering plagioclase (46°36'15.69" N, 90°1'39.43" E; drill hole ZK1204, 432 m depth). **(c)** Quartz veins in the potassic zone containing molybdenite and biotite that has been chlorite-altered, as well as late fissure-filled calcite veinlets (46°36'14.43" N, 90°1'57.86" E; drill hole ZK2403, 1140 m depth). **(d)** Reflected-light photomicrographs of stage IIa chalcopyrite intergrown with euhedral pyrite and biotite (46°36'15.69" N, 90°1'39.43" E; drill hole ZK1204, 432 m depth). **(e)** Stage IIb epidote selectively replacing plagioclase phenocrysts with fine-grained calcite and quartz (CPL; 46°36'6.33" N, 90°1'21.72" E; surface sample at elevation of 1543 m). **(f)** Stage III phyllic alteration with wormy veinlets of chlorite and patches of pyrite (46°36'14.12" N, 90°1'43.25" E; drill hole ZK1606, 680 m depth). **(g)** Stage III quartz veins with muscovite and minor illite-dominated halos replacing secondary K-feldspar (46°36'16.92" N, 90°1'30.78" E; drill hole ZK0405, 159 m depth). **(h)** Stage III fine-grained muscovite and chlorite replacing primary plagioclase and biotite, and secondary biotite (CPL; 46°36'15.69" N, 90°1'39.43" E; drill hole ZK1204, 442 m depth). Abbreviations: Kfs = K-feldspar; Act = actinolite; Pl = plagioclase; Cal = calcite; Bt = biotite; Chl = chlorite; Ep = epidote; Qz = quartz; Ccp = chalcopyrite; Py = pyrite; Mag = magnetite; Mol = molybdenite. Note that the subscripts for Py represent the corresponding paragenetic stage of pyrite. (Color online.)



overprinting, cross-cutting, and alteration mineral assemblages (Fig. 3). Their spatial distributions are displayed in Figure 2.

Stage I: Sodic-calcic alteration

This stage comprises abundant magnetite, actinolite, plagioclase, minor epidote and biotite, and traces of quartz (Fig. 3). Arancibia and Clark (1996) and Sillitoe (2010) interpreted this type of magnetite-actinolite-plagioclase-dominated alteration as

one of the earliest-forming alteration assemblages, implying an oxidized, sulfur-deficient initial fluid. The alteration assemblage is characterized by randomly oriented subhedral to euhedral magnetite grains that replaced primary mafic minerals (e.g., amphibole and biotite) in both the phenocrysts and groundmass of the diorite porphyry (Fig. 4a). The presence of actinolite along with plagioclase (\pm albite) and minor epidote implies the addition of Ca and Na to the host rock. While both magnetite and plagioclase

are abundant in the diorite porphyry, the preservation of primary textures is rare (Fig. 4a). Pyrite occurs as disseminated grains with magnetite and chlorite-altered actinolite. Subhedral pyrite grains contain rare chalcopyrite inclusions and disseminated magnetite along their rims. The sodic-calcic alteration zone at Yulekenhalasu ranges from 10 to 50 m thick and is preserved in the diorite porphyry adjacent to andesitic and basaltic wall rocks (Fig. 2a). It occurs adjacent to the orebody and is poorly mineralized relative to later alteration assemblages.

Stage IIa: Potassic alteration

The potassic alteration zone comprises abundant K-feldspar and quartz, together with lesser biotite, anhydrite, and magnetite, and traces of apatite and titanite (Fig. 3). The reddish potassic-altered diorite porphyry contains fine-grained secondary K-feldspar, quartz, and minor magnetite, which have partially to completely destroyed primary mineral textures (Fig. 4b). K-feldspar and quartz selectively replaced primary feldspars in the groundmass, whereas primary mafic minerals (e.g., amphibole and biotite) were replaced by fine-grained biotite that was subsequently altered locally to muscovite or chlorite. Quartz veins that contain molybdenite and biotite are common in the potassic zone. They have been cut by late calcite veinlets (Fig. 4c). Hypogene Cu mineralization is mainly associated with K-feldspar-dominated potassic alteration, with abundant chalcopyrite occurring as disseminations or veinlets in the host diorite. Euhedral pyrite crystals in this assemblage are commonly surrounded by chalcopyrite (Fig. 4d). Spatially, the majority of hypogene mineralization at Yulekenhalasu is hosted within the potassic-altered diorite porphyry and is adjacent to the underlying porphyritic syenite (Fig. 2a), with the potassic alteration zone accounting for ~90% of Cu metal reserves.

Stage IIb: Propylitic alteration

The propylitic alteration zone, forming a halo around the potassic zone, is inferred to have formed at the same time from the spent fluids from the potassic alteration migrating away from the porphyry center. The zone is characterized by veinlets or aggregate patches of chlorite + pyrite, planar epidote + chlorite, and locally by thick veins (~1 cm) of quartz + gypsum + chlorite in the diorite porphyry and surrounding volcanic wall rocks (Figs. 3 and 4e). Propylitic-altered rocks peripheral to the deposit are commonly dark green and contain alteration assemblages dominated by chlorite, epidote, calcite, quartz, and minor actinolite and gypsum (Fig. 3).

Fine-grained epidote occurs with chlorite, calcite, and minor actinolite and has replaced primary amphibole and plagioclase (Fig. 4e). Chlorite commonly occurs as aggregates or veinlets in the groundmass of the diorite porphyry or pseudomorphs of primary amphibole and biotite crystals. Propylitic alteration is developed along the margin of the sodic-calcic alteration zone and extends through the diorite porphyry to the surrounding andesitic and basaltic wall rocks (Fig. 2a). The propylitic assemblage contains rare, disseminated pyrite grains and no chalcopyrite.

Stage III: Phyllic alteration

The phyllic alteration zone at Yulekenhalasu consists mainly of quartz, pyrite, muscovite, and chlorite, as well as minor illite (Figs. 3 and 4f–4h). Rocks that have undergone phyllic alteration are gray and show partial to complete replacement of primary

plagioclase and mafic minerals (e.g., amphibole and biotite) by secondary muscovite and chlorite, respectively (Figs. 4f–4g). Chlorite occurs locally as wormy veinlets concomitant with pyrite patches (Fig. 4f). The phyllic assemblage is commonly associated with quartz veins up to several centimeters wide that have pervasive halos of muscovite and/or illite. The superposition of phyllic alteration on earlier formed potassic alteration assemblages resulted in the alteration of secondary biotite to chlorite and muscovite (Fig. 4h) and of magnetite to hematite. Pyrite is the dominant sulfide in phyllic-altered rocks and occurs extensively as medium- to fine-grained anhedral nodules. Minor chalcopyrite is present as small inclusions in pyrite. Phyllic alteration at Yulekenhalasu has superimposed on early-formed alteration assemblages, typically at shallower levels relative to deep-seated sodic-calcic and potassic zones (Fig. 2a).

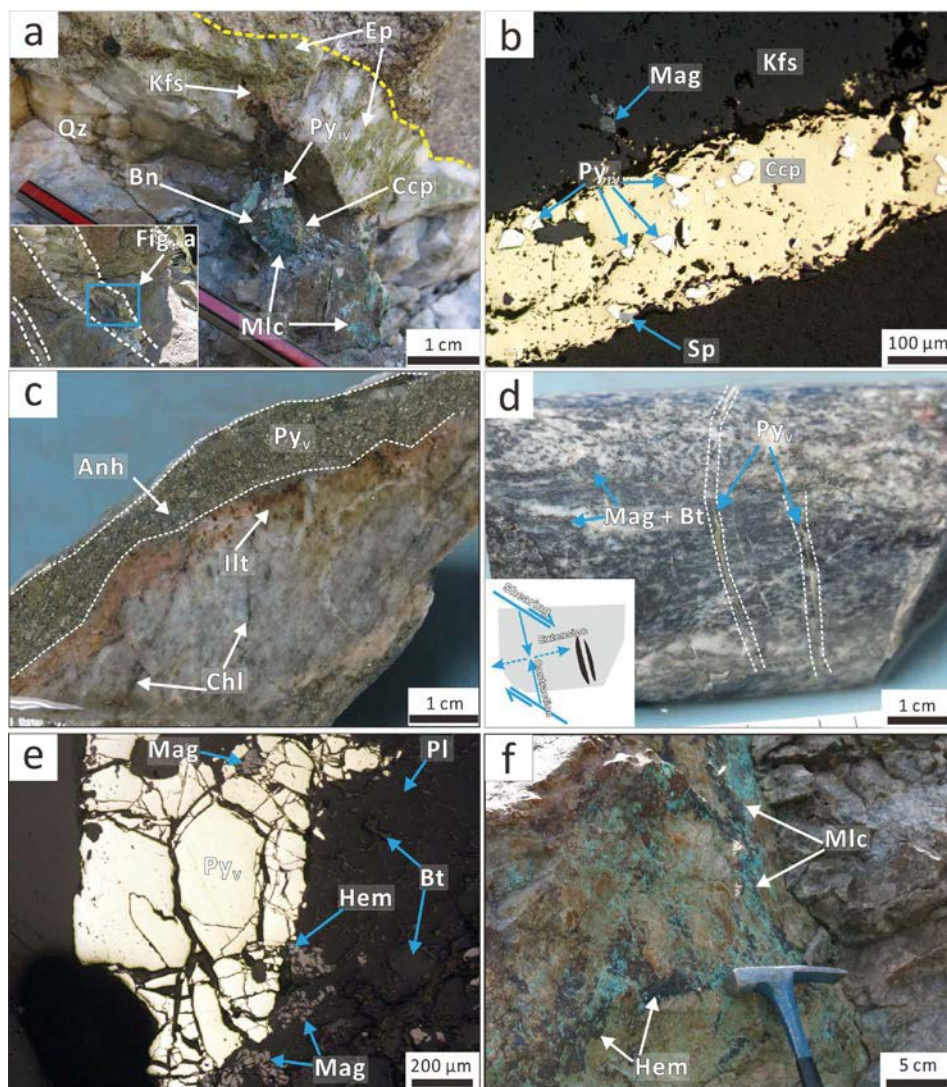
Stage IV: Late Cu sulfide-bearing veins

Widespread late-stage Cu-bearing hydrothermal veins at Yulekenhalasu overprinted earlier alteration assemblages and contributed substantially to the overall Cu resource. They vary from irregular, discontinuous, and segmented to regular, continuous, and parallel veins up to several centimeters wide (Figs. 5a and 5b). They mainly occur in the core of the deposit but, in some cases, occur on the periphery of the potassic zone. The veins are characterized by several assemblages: pyrite + chalcopyrite + anhydrite (Vein a), pyrite + chalcopyrite + sphalerite (Vein b), bornite + pyrite + chalcopyrite (Vein c), and quartz + epidote + K-feldspar + bornite + pyrite + chalcopyrite (Vein d; Fig. 3). All vein types have sharp contacts with the potassic- and phyllic-altered diorite porphyry (Fig. 5a). The lack of associated alteration halos indicates that these Cu sulfide-bearing veins are distinct from Stage III phyllic veins and may have formed by late-stage open-space filling, rather than synchronous with potassic alteration. Euhedral quartz, locally present in some veins, shows undulose extinction and hosts abundant fluid inclusions. Pyrite generally occurs as euhedral crystals without inclusions. Minor sphalerite occurs on the margin of pyrite grains and as isolated crystals in coexisting chalcopyrite (Fig. 5b). The late Cu sulfide-bearing veins are locally responsible for hypogene upgrading and account for roughly 5% of the Cu metal reserves.

Stage V: Argillic alteration

The argillic alteration zone at Yulekenhalasu is characterized by fine-grained quartz, kaolinite, muscovite, and illite, which have completely replaced precursor minerals and destroyed primary textures (Figs. 3 and 5c–5e). Although there is a similarity in mineral assemblages between the phyllic and argillic alteration zones, the transition from phyllic-dominated to argillic-dominated alteration assemblages is characterized by decreasing abundance of chlorite and pyrite and increasing abundance of illite and kaolinite. The argillic alteration zone contains planar pyrite ± galena ± anhydrite ± calcite veins up to several centimeters wide (Figs. 5c–5e). These veins locally developed as fissures cross-cutting potassic alteration assemblages and are orientated along the tensile fractures caused by dextral shearing (Fig. 5d). Pyrite in these veins occurs as subhedral to euhedral crystals with occasional magnetite inclusions (Fig. 5e). Although the similarities in mineral assemblages between the phyllic and argillic alteration zones make it difficult

FIGURE 5. Representative photographs and photomicrographs of late stage and supergene alteration and mineralization assemblages at Yulekenhalasu. (a) Stage IV sheeted veins cutting potassic and propylitic altered rocks and containing quartz, epidote, K-feldspar, bornite, pyrite, and chalcopyrite. The inset figure illustrates the field distributions of the specimens (46°36'1.68" N, 90°1'31.36" E; surface sample at elevation of 1531 m). (b) Stage IV chalcopyrite vein with euhedral pyrite grains that injected potassic altered diorite porphyry (46°36'18.06" N, 90°1'47.01" E; drill hole ZK1607, 787 m depth). (c) Stage V pyrite, anhydrite, and calcite occurring in a shear plane (46°36'14.43" N, 90°1'57.86" E; drill hole ZK2403, 1146 m depth). (d) Argillic alteration overprinting potassic alteration, with sheeted pyrite veins produced by dextral shearing during stage V and inset figure outlining internal tectonic stress (46°36'14.43" N, 90°1'57.86" E; drill hole ZK2403, 1159 m depth). (e) Stage V showing pyrite veins with local relict of magnetite inclusions, indicating that stage V overprinted potassic alteration (46°36'14.43" N, 90°1'57.86" E; drill hole ZK2403, 1159 m depth). (f) Stage VI supergene alteration with hematite and malachite present along fracture plane (46°36'9.93" N, 90°1'30.54" E; surface sample at elevation of 1537 m). Abbreviations: Kfs = K-feldspar; Chl = chlorite; Ep = epidote; Qz = quartz; Illt = illite; Bt = biotite; Anh = anhydrite; Ccp = chalcopyrite; Py = pyrite; Mag = magnetite; Bn = bornite; Hem = hematite; Mlc = malachite; Sp = sphalerite. (Color online.)



to define the boundary between them at depth, argillic alteration near-surface is generally restricted to shear zones parallel to the NNW-trending fault system in the eastern mineralized zone (Figs. 2b and 2c) and to the NW-trending fault system in the western zone (Fig. 2b), where it is separated from the phyllic alteration zone by a sharp faulted contact (Fig. 2d).

Supergene alteration

Most mineralized rocks at Yulekenhalasu exposed at the surface or at shallow depths have been subjected to supergene oxidation processes (Yang et al. 2014), with hematite, malachite and minor jarosite and covellite commonly replacing primary sulfides (Fig. 3). Supergene enrichment at Yulekenhalasu extends tens of meters deep locally and is particularly intense in strongly faulted areas with substantial malachite mineralization at fault contacts (Fig. 5f).

PYRITE COMPOSITION

Sampling

To help constrain the chemical evolution of the hydrothermal fluids and assist in paragenetic interpretation, representative pyrite grains were analyzed from several alteration and mineralized zones at Yulekenhalasu. The samples analyzed include four from the sodic-calcic alteration zone (Py_i; Fig. 4a), six from the potassic zone (Py_{IIa}; Figs. 4b–4c), five from the propylitic zone (Py_{IIb}), 12 from the phyllic alteration zone (Py_{III}; Figs. 4f–4g), four from late Cu sulfide-bearing veins (Py_{IV}; Fig. 5a), and two from the argillic alteration zone (Py_V; Figs. 5c–5d). To compare magmatic-hydrothermal pyrite composition with pyrite of sedimentary origin, three examples of pyrite characterized by microcrystalline pyrite aligned parallel to bedding texture in the overlying sedimentary

FIGURE 6. Comparative box plot of log-base-10-transformed trace elemental concentrations in pyrite from sodic-calcic alteration (Py_I), potassic stage (Py_{IIa}), propylitic stage (Py_{IIb}), phyllic stage (Py_{III}), late Cu sulfide-bearing veins (Py_{IV}), and argillic assemblages (Py_V). Pathfinder elements are highlighted by yellow background. Note that data of Py_S from the sedimentary rocks of Jiangbasitao Formation that noncontinuously overlay Yulekenhalasu are included for comparison. (Color online.)

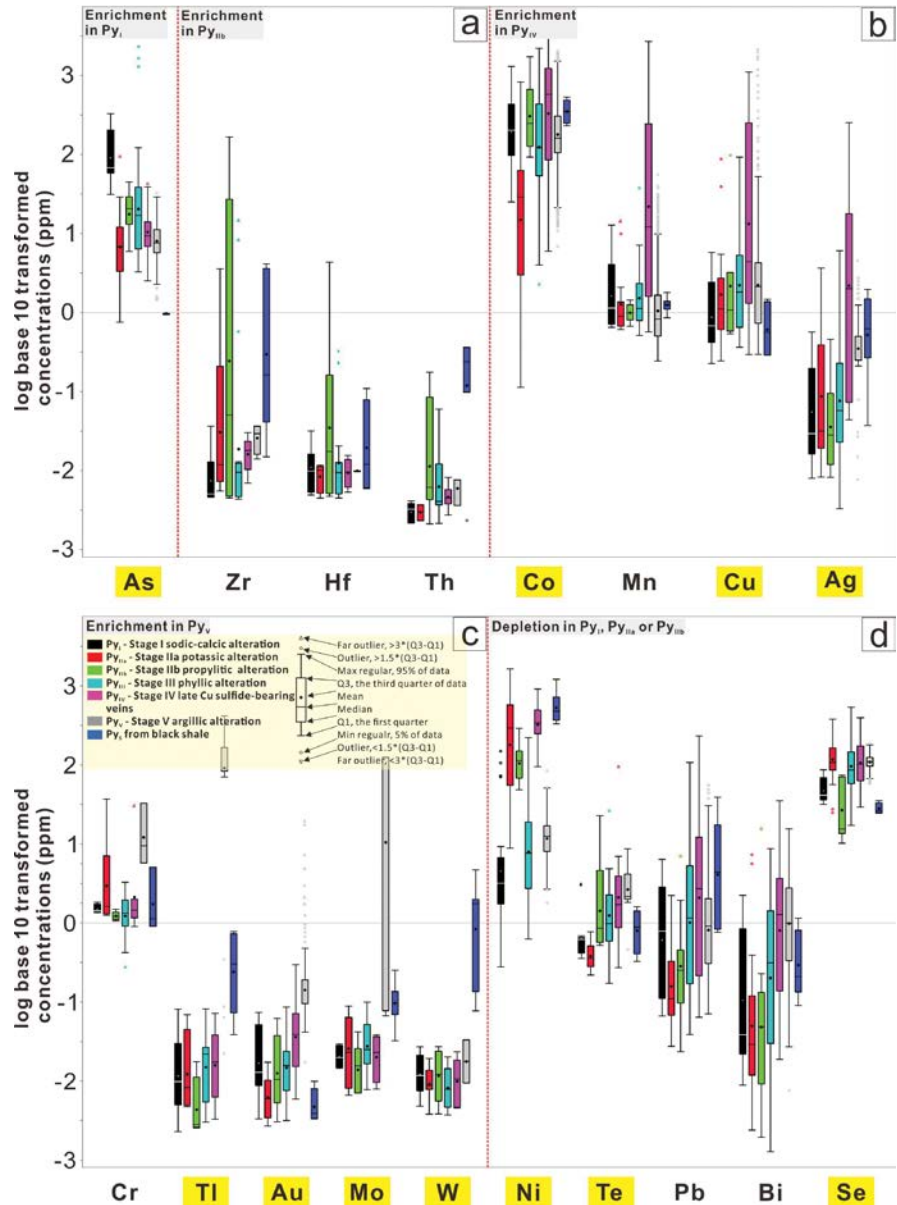
rocks of the Jiangbasitao Formation were also analyzed (Py_S).

LA-ICP-MS analysis method

All selected pyrite grains were analyzed at the LA-ICP-MS facility at CODES, University of Tasmania, using a RESOLUTION laser platform equipped with a Coherent COMPex Pro 193 nm excimer laser and Lauren Technic S155 large format sample cell, coupled to an Agilent 7700 or 7900 quadrupole ICP-MS. Laser spot size is 29 μm for all pyrite and 51 μm for STDGL3 standard glass. A combination of spot analysis and elemental mapping generated by rastering a focused laser beam across the mineral surface was attempted. To calculate concentrations, the average of the signal over the time interval of interest is calibrated against reference standard STDGL3, an in-house standard sulfide-rich glass for primary calibration for quantifying siderophile and chalcophile elements (Danyushevsky et al. 2011). Data reduction and processing of the laser images were performed using CODES in-house routines. The error on average that is estimated from the standards is <5%, which was insignificant in comparison to the samples because the majority of analyzed elements in pyrite showed several orders of magnitude variation in concentration. Full analytical details are provided in Online Materials¹ OM1.

RESULTS

Representative pyrite major and trace element concentrations (S, Co, Se, Ni, As, Ti, Cr, Cu, Mn, Zn, Te, Pb, Mg, Sb, Bi, Sn, Ag, V, Cd, Mo, Tl, Gd, Au, Zr, Hf, W, Nb, Th, U, and Ta) are listed in Online Materials¹ OM2 and illustrated in part in Figure 6. It should be noted that ~2000 inclusion-free data points for argillic Py_V acquired from elemental mapping



following the studies of Acosta-Góngora et al. (2022) and Sykora et al. (2018) are added to the data set for comparison.

Paragenetic variations of pyrite composition

Comparison of trace element variability in pyrite across all hydrothermal alteration stages at Yulekenhalasu indicates that Py_{IV} and Py_V have relatively high concentrations of pathfinder trace elements, e.g., Co, Ni, As, Sb, Se, Cu, Ag, Tl, Au, Te, Mo, and W (Fig. 6), which may provide vectoring information to the locus of porphyry mineralization (Cooke et al. 2014; Sykora et al. 2018). Moreover, Py_S hosted in sedimentary rocks show remarkable enrichment in Th, Mo, and W relative to hydrothermal pyrites at Yulekenhalasu. They are interpreted to be of sedimentary origin based on their microcrystalline texture aligned parallel to bedding and Co/Ni values below

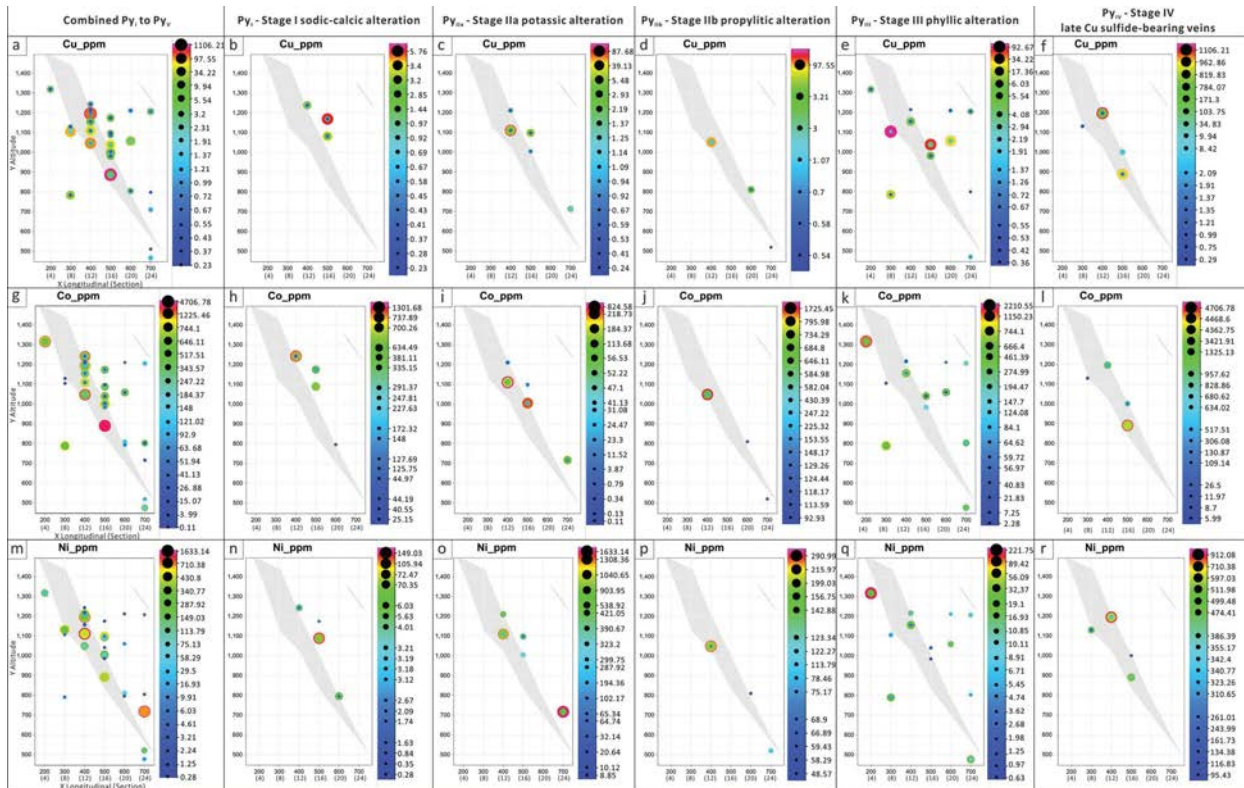


FIGURE 7. Spatial variations of Cu, Co, and Ni in pyrite in a series of NE-SW cross sections of Yulekenhalasu: Trace element contents for combined and individual paragenetic stages (Py_I to Py_{IV}). X-axis relates to sample location in drillcore. Gray shades represent the ore-body projected onto the longitudinal section. (Color online.)

2 (cf. Large et al. 2014). Trace element concentrations in the various paragenetic stages of pyrite show some distinctive traits with enrichment of As in sodic-calcic alteration, Ti, Zr, Gd, Hf, Th, U, and Nb in propylitic alteration, Co, Mn, Cu, Ag, Zn, Sn, and V in late Cu sulfide-bearing veins, and Cr, Tl, Au, Mo, W, and Sb in argillic alteration (Fig. 6; Online Materials¹ OM2). Ni is depleted in pyrite from sodic-calcic alteration, Te is characteristically depleted in sodic-calcic and potassic pyrite, Pb and Bi are depleted in potassic and propylitic pyrite, and Se is depleted in propylitic pyrite relative to the measured abundances in other alteration stages (Fig. 6). In general, Py_{III} has trace element compositions that range between early porphyry and late vein stages, without notable enrichment or depletion compared to other pyrite types.

Spatial variation in pyrite composition

Representative trace element abundances in pyrite for each hydrothermal stage have been plotted spatially on longitudinal sections in Figure 7 (Cu, Co, and Ni) and Online Materials¹ OM3 (As, Se, and Au). It should be noted that no spatial trends could be identified for elements in stage V (argillic alteration), due to the limited data available for these longitudinal sections. To evaluate the enrichment or depletion of elements around the deposit center, we developed a quantitative method to evaluate the distances of sampling locations to the orebody. Specifically, the spatial extent of the orebody is simplified as an ellipse in sections, and the sum

of distances of certain sampling locations to two focus points of the defined ellipse serves as the quantitative measurement of proximity to the orebody. Consequently, high-distance values are distal to the deposit center and low-distance values are proximal, as illustrated in the schematic diagram (Fig. 8a). Spatial trends of analyzed elements in different paragenetic stages, which are highlighted by dotted arrows, are revealed by the average and median values of analyses from the same sample (Figs. 8b–8f; Online Materials¹ OM4).

Among pyrite of stages I–IV, Cu is the main element whose concentration appears associated with mineralization. It has high concentrations (>10 ppm) in pyrite near the deposit center in paragenetic stages IIa (Figs. 7c and 8b), IIb (Figs. 7d and 8c), and III (Figs. 7e and 8d). Cobalt also has high concentrations in pyrite close to the deposit center, particularly in stages IIa (Figs. 7i and 8e) and IIb (Figs. 7j and 8f), but not in stages I (Fig. 7h; Online Materials¹ OM4a), III (Fig. 7k; Online Materials¹ OM4b), or IV (Fig. 7l; Online Materials¹ OM4c). Nickel has a similar spatial enrichment pattern to Co in stage IIb (Figs. 7j, 7p, and 8f; Online Materials¹ OM4d), but differs for stage IV (Fig. 7r; Online Materials¹ OM4e), where the highest Ni concentrations occur at shallow levels relative to Co (Fig. 7i; Online Materials¹ OM4c).

Arsenic is distinctly enriched in pyrite at deeper levels in stages IIa (Online Materials¹ OM3c and OM4f) and IV pyrites (Online Materials¹ OM3f and OM4g). Selenium is enriched in the peripheral zone (>800 m away from center) surrounding the

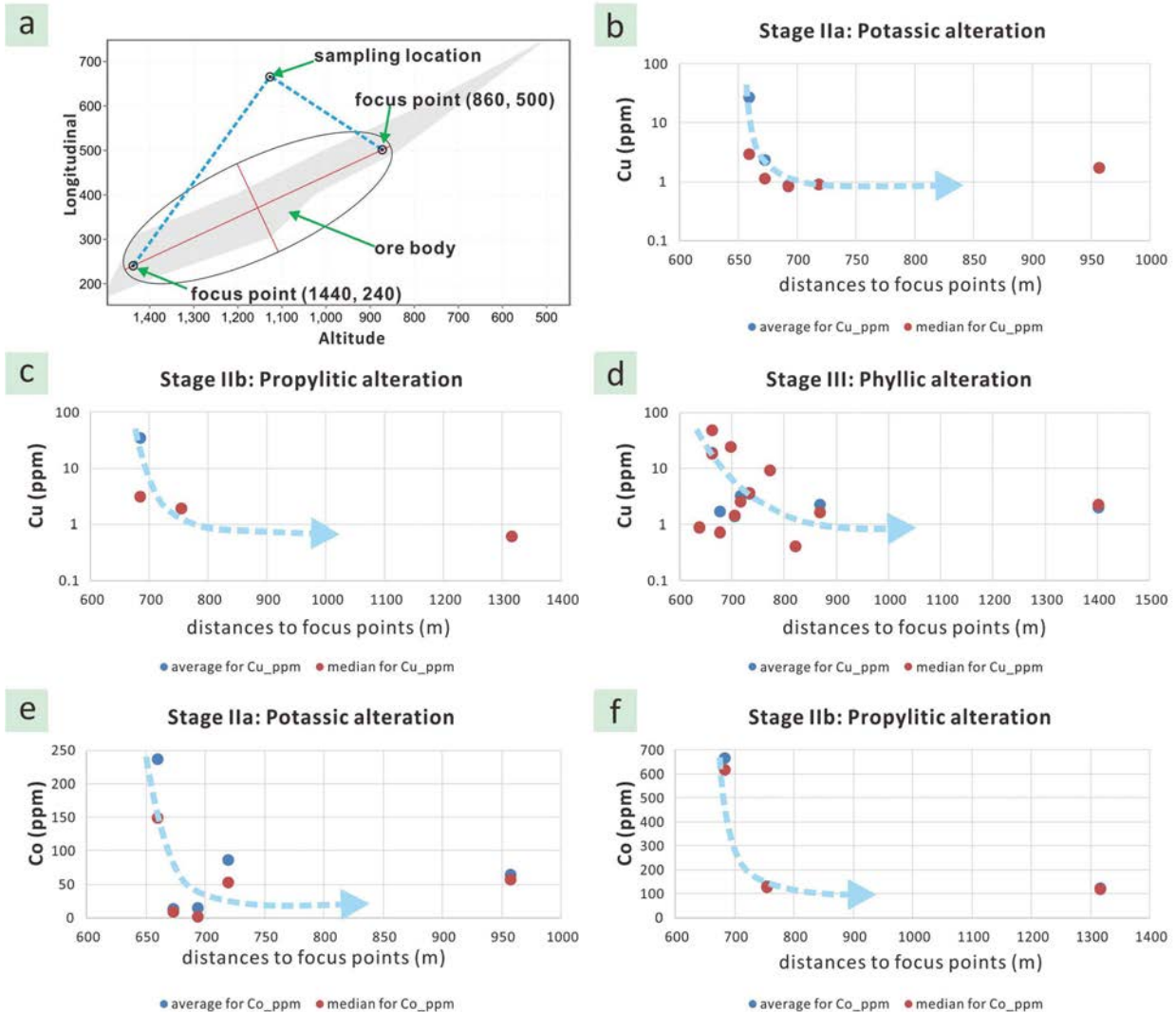


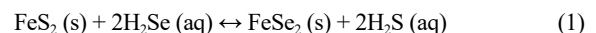
FIGURE 8. Schematic diagram for the quantitative method to evaluate the distances of sampling locations to the orebody (a) and spatial trends of Cu and Co in porphyry-type alteration stages (b–f). (Color online.)

deposit center in stages IIb (Online Materials¹ OM3j and OM4h) and III (Online Materials¹ OM3k and OM4i), whereas high-Se concentrations occur proximal to the ore body in stages I (Online Materials¹ OM3h and OM4j) and IIa (Online Materials¹ OM3i and OM4k). Similar trends were also noted for Au (Online Materials¹ OM3m–OM3r, OM4l, and OM4m), except in stage IIb (Online Materials¹ OM3p and OM4n), where high-Au concentrations are present proximal to the deposit center.

Determination of fluid compositions by pyrite geochemistry and temperatures

Selenium is one of the most abundant elements occurring as a stoichiometric substitution for sulfur in pyrite (Diener et al. 2012; Keith et al. 2018; Layton-Matthews et al. 2008). Although the aqueous geochemistry of Se was discussed by D'yachkova and Khodakovskiy (1968) and Yamamoto (1976), the influence of temperature and hydrothermal fluid compositions on Se incorporation into pyrite remains unclear. Temperature has been

interpreted to have either a positive effect on Se concentrations in pyrite (i.e., high temperature favors high-Se concentration in pyrite) (Layton-Matthews et al. 2008; Tischendorf 1966; Wohlgenuth-Ueberwasser et al. 2015) or a negative effect (i.e., high temperature favors low-Se concentration in pyrite) (Hawley and Nichol 1959; Huston et al. 1995; Lorand et al. 2003). To determine the behavior of Se in pyrite, we conducted modeling based on reaction 1 as described by Huston et al. (1995), with modeled ratios of H_2Se/H_2S in fluid illustrated in Figure 9. The full detailed process of Se/S modeling and scalar calculations is provided in Online Materials¹ OM1. The balanced equation for reaction 1 from Huston et al. (1995) is:



As shown in Figure 9a, the molar ratios of Se/S in pyrite generally decrease with increasing temperature under a constant ratio of Se/S in the fluid when equilibrium balance is reached.

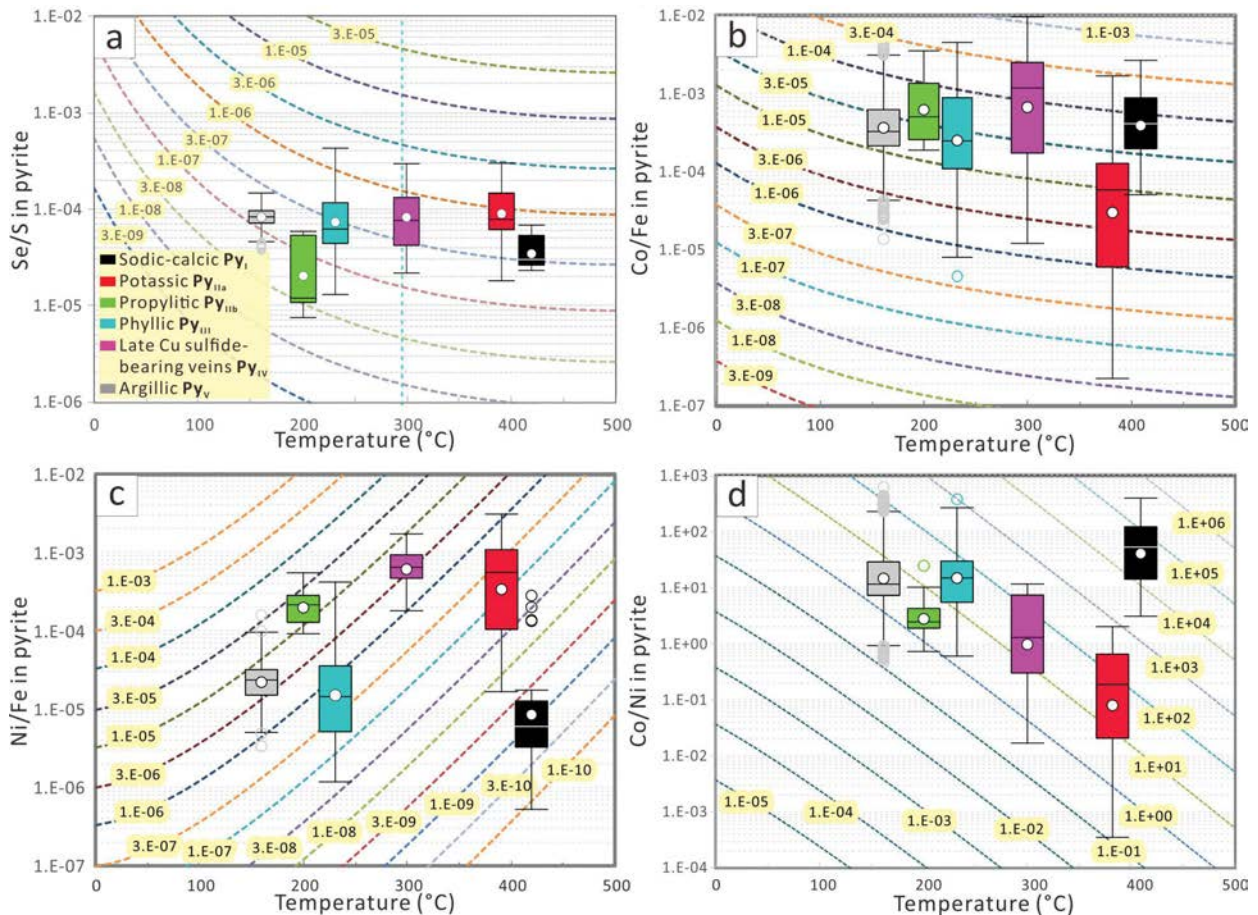
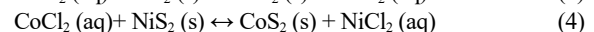
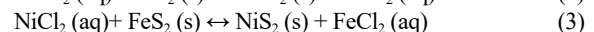
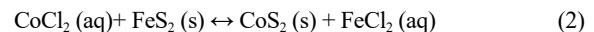


FIGURE 9. Correlations between trace element ratios in pyrite and estimated values in hydrothermal fluids as a function of temperature. The dash curves in each panel represent the hydrothermal fluids with constant elemental ratios labeled by overlapped numbers with yellow backgrounds. (a) Temperature dependence of Se/S in pyrite. Note that Se/S in pyrite increases with $m_{\text{Se}}/m_{\text{S}}$ of fluid but decreases with temperature. (b) Temperature dependence of Co/Fe in pyrite. (c) Temperature dependence of Ni/Fe in pyrite. (d) Temperature dependence of Co/Ni in pyrite. Corresponding hydrothermal $m_{\text{Se}}/m_{\text{S}}$ values are estimated based on the temperatures of ~ 410 °C for sodic-calcic alteration (Wu et al. 2019), ~ 400 °C for potassic alteration, ~ 200 °C for propylitic alteration, ~ 230 °C for phyllic alteration, ~ 300 °C for late Cu sulfide-bearing veins and ~ 160 °C for argillic alteration stages (Wu 2018; Table 1). (Color online.)

Moreover, at temperatures below 300 °C, Se/S in pyrite is dominated by both temperature and Se/S in hydrothermal fluid, but the influence of temperature becomes negligible above 300 °C (Fig. 9a), which may explain the geological observations of the non-uniform temperature dependence of Se in pyrite. Because Se concentrations in pyrite can record the Se of parental hydrothermal fluid (Huston et al. 1995), combining our measured Se concentrations in pyrite with the fluid inclusion results of Wu (2018) can provide rough estimates of Se/S ($\sim 3 \times 10^{-8}$ to 1×10^{-6}) in the hydrothermal fluids (Fig. 9a).

The ratio of Co/Ni in pyrite has long been used as an indicator for ore genesis (Bajwah et al. 1987; Bralía et al. 1979; Loftus-Hills and Solomon 1967). Due to the apparent dependence of Co/Ni on various factors, e.g., temperature, fluid composition, and ore-forming processes (Bajwah et al. 1987; Bralía et al. 1979; Campbell and Ethier 1984; Loftus-Hills and Solomon 1967), the use of Co/Ni requires supporting evidence to help interpret magmatic-hydrothermal processes in the ore-forming environment.

Based on a similar hypothesis to Se substitution in pyrite, we proposed a novel approach to link Co and Ni contents in pyrite to their compositions in the mineralizing fluids (Online Materials¹ OM1). First, the partition dependence of Co and Ni between the hydrothermal fluid and coexisting pyrite with temperature has been estimated using reactions 2, 3, and 4, assuming that Fe, Co, and Ni are transported primarily as chloride complexes (Fig. 9).



Reactions 2–4 have been used to calculate Co/Fe, Ni/Fe, and Co/Ni for the hydrothermal fluids at Yulekenhalasu, using the results of the fluid inclusion study of Wu (2018). As illustrated in Figures 9b and 9c, Ni and Co concentrations in pyrite appear to increase along with Ni/Fe and Co/Fe in the hydrothermal fluid. An increase in temperature will decrease Co contents and increase Ni contents in pyrite (Figs. 9b–9c), causing Co/Ni in pyrite to increase with decreasing temperatures (Fig. 9d).

DISCUSSION

Trace element substitution and correlations in pyrite

Trace elements can be incorporated into the pyrite crystal structure through stoichiometric lattice substitution, non-stoichiometric substitution, and as micro- or nano-inclusions (Huston et al. 1995; Keith et al. 2016, 2018; Large et al. 2014; Reich et al. 2013; Sykora et al. 2018). From time-resolved LA-ICP-MS spectra of pyrite (Fig. 10), Co and Ni concentrations are typically parallel to Fe concentrations, consistent with Co and Ni occurring within the pyrite crystal lattice and substituting for Fe in a stoichiometric manner (Huston et al. 1995). However, several pyrite analyses from Yulekenhalasu showed abrupt changes in intensity for Co or Ni in time-resolved depth profiles, indicating the presence of discrete growth zones of Co or Ni as stoichiometric lattice substitution in pyrite (Figs. 10a–10c). Both As and Se are commonly present in measurable concentrations in pyrite and can substitute for S in the crystal lattice (Abraitis et al. 2004; Zhou et al. 2010). Huston et al. (1995) concluded that As is incorporated into pyrite as a non-stoichiometric substitution, in contrast to Se, which occurs as a stoichiometric substitution.

The abrupt changes in element counts for Cu, Pb, and Zn in the time-resolved spectra for some pyrite analyses (Figs. 10c and 10d) indicate the presence of nano- or micro-inclusions in pyrite; i.e., chalcopyrite and tetrahedrite-tennantite series inclusions for Cu, galena inclusions for Pb, and sphalerite inclusions

for Zn (Huston et al. 1995; Large et al. 2014; Reich et al. 2013). Positive correlations of Bi with Cu, Pb, and Ag (Figs. 11a–11c) suggest the presence of Bi-rich or Bi-bearing tetrahedrite and galena (Abraitis et al. 2004). Gold shows a positive correlation with Bi and Te (Figs. 11e–11f), but no correlation with As (Fig. 11g), highlighting a potential role for Bi and/or Te complexes in the transport of Au in magmatic-hydrothermal systems (Acosta-Góngora et al. 2015; Cook et al. 2009). Consequently, Au is most likely occurring as micro- or nano-inclusions of Au telluride or bismuthide in pyrite (Reich et al. 2013).

Paragenetic and spatial variation of trace elements in pyrite

A LA-ICP-MS element map of a composite pyrite grain that has a core of Py_{IIa} (potassic alteration) and a rim of Py_V (argillic alteration) is shown in Figure 12. The texture of Py_{IIa} is well preserved despite the overprinting of Py_V, implying that the trace elements in Py_{IIa} have not been mobilized by subsequent alteration events. Elemental zoning in Py_{IIa} is interpreted to be related to contamination by silicates based on the correlation between high-Al contents and mineral inclusions in pyrite (Figs. 12b and 12c). As illustrated in Figure 9d, Co/Ni in hydrothermal fluid for Py_{IIa} (median of 20) is higher than that for Py_V (median of 4). The lower Co/Ni values in Py_{IIa} (median of 0.2) than in Py_V (median of 10) are attributed to the higher crystallizing temperature of Py_{IIa} (~400 °C) compared to Py_V (~160 °C; Fig. 9d), because increasing temperatures would have a negative affect on Co/Ni ratios in pyrite

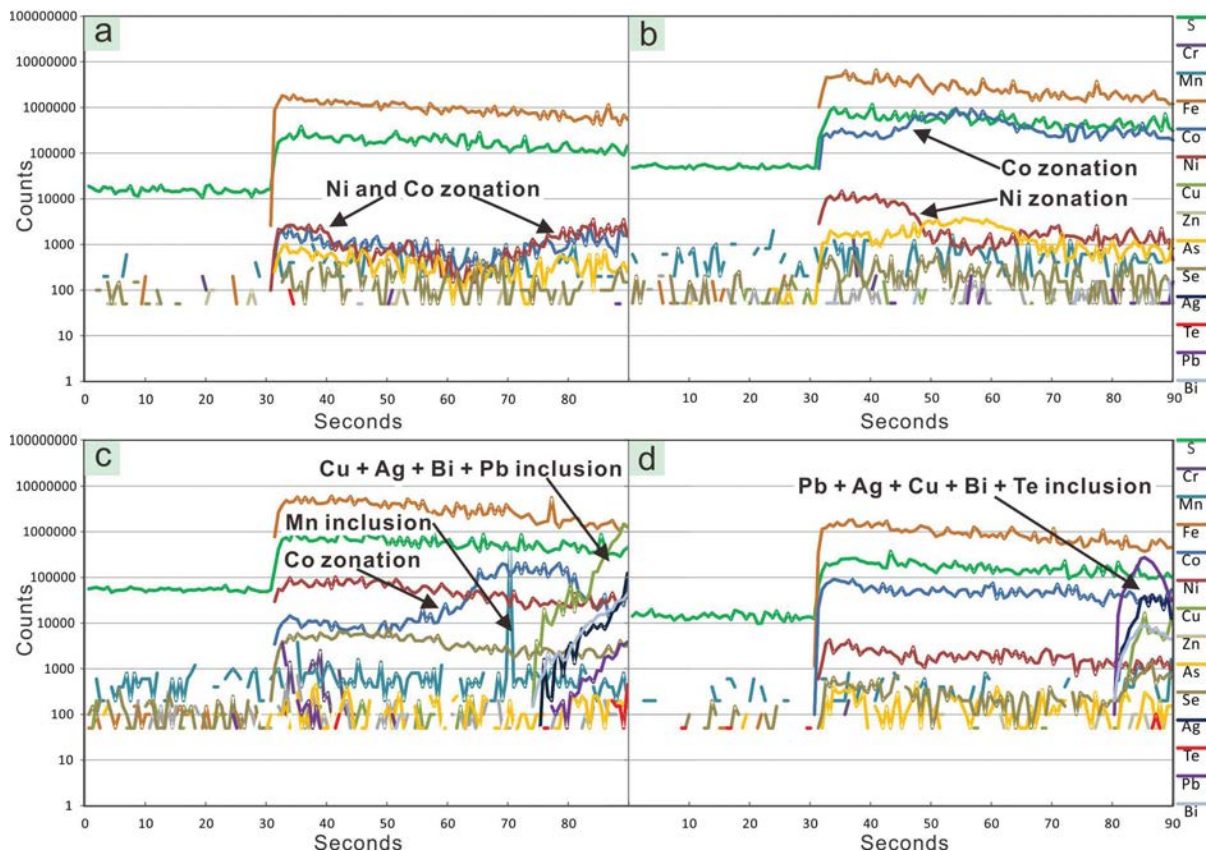


FIGURE 10. Representative time-resolved depth profiles, demonstrating concentrations (in counts per second) of S, Cr, Mn, Fe, Co, Ni, Cu, Zn, As, Se, Ag, Te, Pb, and Bi in pyrite samples from Yulekenhalasu. Note the stair-step pattern of Co and Ni reflecting chemical zoning. (Color online.)

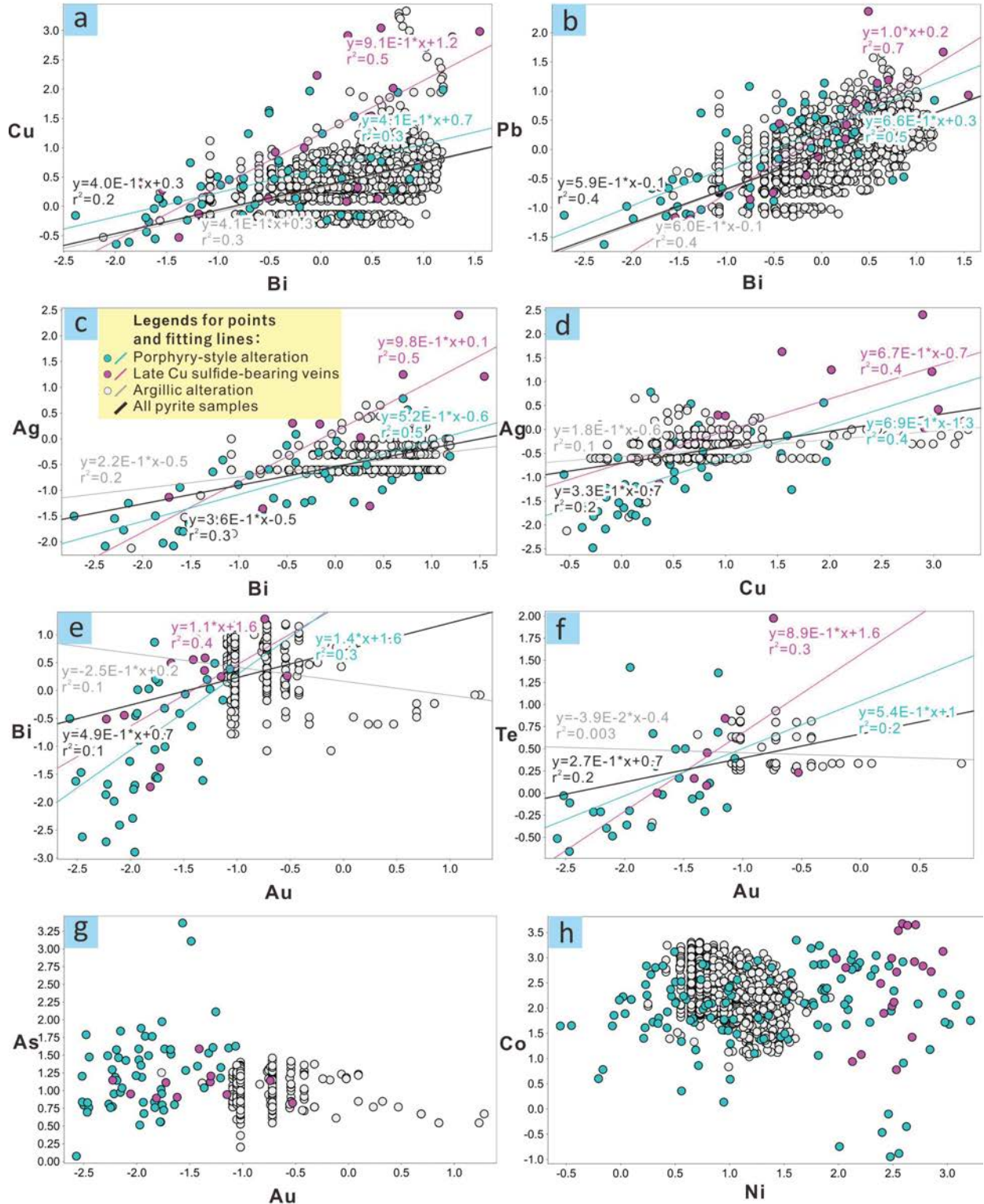
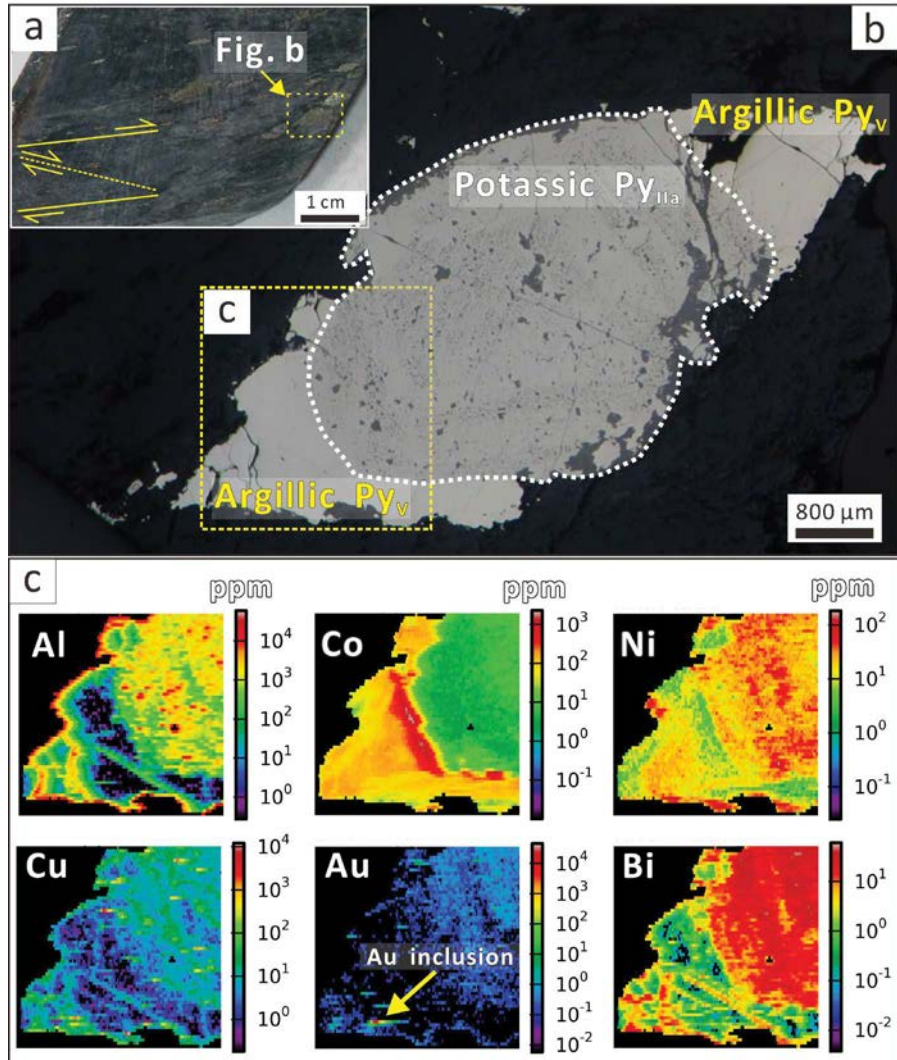


FIGURE 11. LA-ICP-MS analysis of pyrite from Yulekenhalasu. (a) Bi vs. Cu, (b) Bi vs. Pb, (c) Bi vs. Ag, (d) Cu vs. Ag, (e) Au vs. Bi, (f) Au vs. Te, and (g) Au vs. As. The log base 10 transformation has been applied to all data points. Fitting lines, calculated by the method of least squares with r^2 values, are provided for porphyry-style alteration, late Cu sulfide-bearing veins, argillic alteration, and all data, respectively. All data are listed in Online Materials¹ OM2. (Color online.)

FIGURE 12. LA-ICP-MS image of potassic-stage pyrite grains (Py_{IIa}) overgrown by argillic-stage pyrite (Py_{V}). Inset figure (a) outlines the area of the specimens of Py_{IIa} with dextral shear deformation; (b) reflected-light image of pyrite grain consisting of the core of Py_{IIa} and the rim of Py_{V} ; (c) LA-ICP-MS images for Al, Co, Ni, Cu, Au, and Bi. (Color online.)



(Fig. 9d). The map highlights that Cu has lower concentrations in Py_{V} than Py_{IIa} (Fig. 12c). There are Au inclusions in Py_{V} (Fig. 12c), which may explain the presence of Au mineralization in argillic altered rocks.

Fluids associated with sodic-calcic alteration (stage I) have similar Se/S compared to the potassic stage, suggesting a similar origin for their hydrothermal fluids (Fig. 9a). The Se/S of stage IV fluids broadly overlap with I and IIa (Fig. 9a), and are systematically higher than those of stages IIb, III, and V. These observations, combined with the involvement of meteoric water in forming stage III, suggest that the hydrothermal fluid responsible for the stage IV late Cu sulfide-bearing veins is similar to stages I and IIa and is also of magmatic-hydrothermal origin.

Ni and Co concentrations in pyrite appear to show significant variations across different paragenetic stages (Fig. 11h). The hydrothermal fluids responsible for sodic-calcic alteration were characterized by higher Co/Ni and Co/Fe but lower Ni/Fe than the potassic stage fluids (Figs. 9b-9d). The increase of Ni/Fe from sodic-calcic to potassic alteration could be explained by a decrease of Fe caused by magnetite crystallization during potassic alteration. The decline in Co/Fe during potassic alteration is possibly controlled by aqueous dispersion of Co, considering the high solubility of Co chloride complexes in the fluid compared to Ni (Acosta-Góngora et al. 2014; Liu et al. 2012). Higher Ni contents in pyrite are typical in mafic host rocks (Bajwah et al. 1987; Botinelly et al. 1985), suggesting that higher Ni/Fe in stage IV relative to stages I and IIa could be a result of hydrothermal fluids derived from or interacting with a mafic source during stage IV (Zhao et al. 2011). This mafic source may have been an intrusive analog from regional Carboniferous units such as the Jiangbasitao Formation and Heishantou Formation (Wang and Xu 2006).

Pyrite from stages I and IIa, which formed at high temperature (Wu 2018), are depleted in most trace elements (Fig. 6), probably due to the slow growth rate for pyrite in high-temperature environments, which allows trace elements to be incorporated

into other sulfide phases rather than concentrated in pyrite (Large et al. 2009). Trace elements enriched in pyrite from propylitic alteration are dominated by lithophile elements (e.g., Ti, Zr, Gd, Hf, and Th), possibly reflecting their incorporation during the rapid growth of pyrite grains in the lower-temperature environment (Large et al. 2009, 2011; Melekestseva et al. 2014). Lower-temperature conditions may have contributed to the enrichment of lithophile elements in Py_{S} (e.g., Zr, Hf, Th, Mo, W, and Tl; Fig. 6). This is because pyrite of sedimentary origin also tends to be contaminated by silicate micro-inclusions (e.g., silicate minerals that are more enriched in lithophile elements than pyrite) during the rapid growth of sulfides (Large et al. 2014). The enrichment of Cu, Bi, and Ag in stage IV pyrite implies deposition from a fertile metallogenic hydrothermal fluid (Melekestseva et al. 2014), which is consistent with the sulfide-rich mineral assemblages in stage IV veins. The remarkable enrichment of low-temperature distal pathfinder elements such as Te, Au, and Tl in stage V pyrite is inferred to be related to a low temperature of formation, as indicated by the associated low-temperature ($\sim 160^\circ\text{C}$) fluid

inclusion assemblages and dark-cathodoluminescence quartz (Wu 2018) in argillic alteration (Figs. 3 and 5c).

Copper is concentrated in pyrite proximal to centers of mineralization at Yulekenhalasu (Figs. 9c–9e; Online Materials¹ OM4b–OM4n), implying that ore-forming fluid compositions are the critical factor in producing high concentrations of ore-forming elements in pyrite (Reich et al. 2013), although temperature and other factors cannot be excluded. High-Au concentrations occur distal to the ore body in stage III pyrite (Online Materials¹ OM2q and OM3s) and may suggest that Au precipitates further from the hydrothermal center than Cu. The spatial distribution pattern for Se in pyrite shows high concentrations close to the orebody in stages I (Online Materials¹ OM3h and OM4j) and IIa (Online Materials¹ OM3i and OM4k), but low concentrations close to orebody in stages IIb (Online Materials¹ OM3j and OM4h) and III (Online Materials¹ OM3k and OM4i). For stages I and IIa with temperatures above 300 °C, the curves in Figure 9a change to horizontal, indicating that temperature has a negligible impact on the Se content in pyrite, whereas increased Se/S in the hydrothermal fluid from 3×10^{-7} to 1×10^{-6} could account for high-Se in pyrite close to orebody (Online Materials¹ OM3h, OM3i, OM4j, and OM4k). However, for stages IIb and III pyrite, which formed below 300 °C (Wu 2018), the corresponding curves in Figure 9a are steep, indicating that temperature has a significant inverse effect on Se concentrations in pyrite formed during these stages. Lower Se concentrations in pyrite formed close to the orebody (Online Materials¹ OM4h and OM4i) are possibly due to the relatively higher temperature present in the center of mineralization (Huston et al. 1995).

Genetic model

Porphyry-type alteration and mineralization. The intimate spatial relationship between Devonian diorite porphyry stocks and porphyry-type mineralization at Yulekenhalasu suggests a genetic link that is supported by geochronology (Wu et al. 2015; Yang et al. 2014). The hydrous syn-mineralization diorite porphyry was a product of magmatism triggered by the flat subduction of the

Paleo-Asian ocean plate beneath the Junggar arc (Wu et al. 2015). Flat subduction created a thickened crust that formed the hydrous syn-mineralization magma (Loucks 2014; Wu et al. 2015). The nature of low temperature (ca. 675 °C by Ti-in-zircon temperature) and high oxygen fugacity (FMQ+3 by zircon oxybarometer) in ca. 377 Ma syn-mineralization magma (Wu et al. 2015), prevents the escape of chalcophile elements as sulfide and makes the diorite porphyry a favorable source for porphyry mineralization (Fig. 13a).

Combined with the mineral assemblages in stages I and IIa, the similar Se/S for the sodic-calcic and potassic stage fluids are consistent with fluids for both stages being derived from the diorite porphyry. Propylitic alteration spatially extends from the diorite porphyry into andesitic and basaltic wall rocks, recording the migration of hydrothermal fluids outwards from the locus of magmatic-hydrothermal activity (Fig. 4a; Cooke et al. 2014). Propylitic pyrite is enriched in lithophile elements (Fig. 6) due to rapid growth and assimilation of silicate phases at lower temperatures (~200 °C; Table 1). Phyllic alteration was superimposed onto early-formed porphyry-type alteration (Figs. 2a, 4g, and 4h), with higher Ni/Fe in stage III compared to paragenetic stages I and IIa (Fig. 9c) interpreted to result from dispersion of Fe, indicated by the absence of magnetite or hematite (Fig. 3). The high Ni/Fe in propylitic alteration stage (Fig. 8c) suggests the interaction between hydrothermal fluids and basaltic wall rock which may have contributed more Ni than Fe to fluids.

Post-porphyry stage alteration and mineralization.

Porphyry-type alteration at Yulekenhalasu was overprinted by stage IV Cu sulfide-bearing veins (Figs. 5a–5b) and then by stage V argillic assemblages (Figs. 5d–5e). Pyrite compositions, combined with microthermometric data (Table 1) and cathodoluminescence imaging (Wu 2018), imply that late Cu sulfide-bearing veins (stage IV) were deposited at temperatures around 234–317 °C from CO₂-rich fluids, along with high concentrations of chalcophile elements.

The origin for stage IV mineralization could be attributed to (1) remobilization of preexisting mineralization for the porphyry deposit during orogenesis (e.g., Cairns et al. 2003; Li et al. 2012);

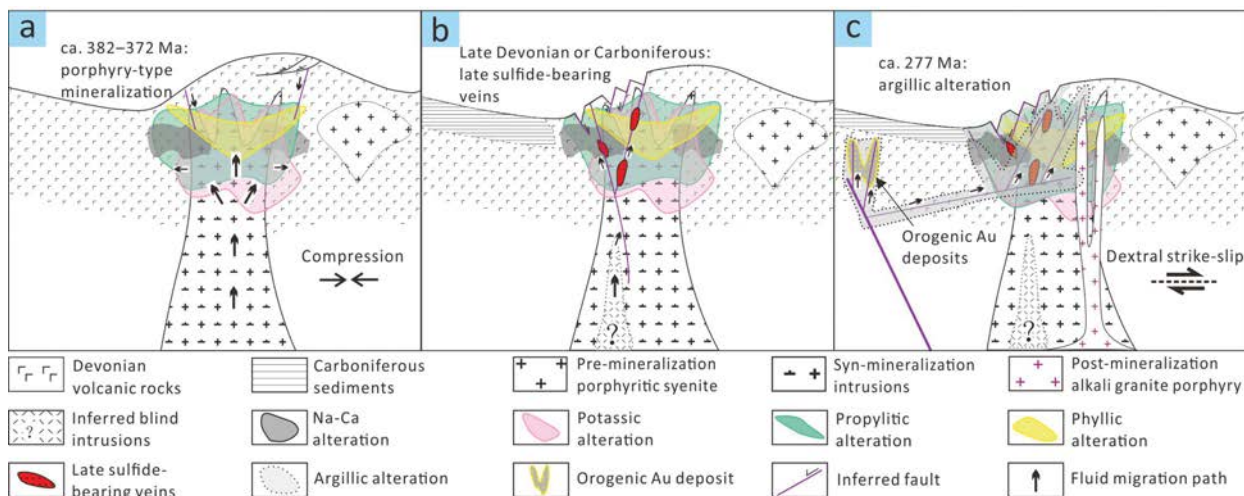


FIGURE 13. Metallogenic model for the formation of the Yulekenhalasu Cu deposit. (a) Flat subduction generated the diorite porphyry and related stage I–III alteration and mineralization at ca. 382–372 Ma. (b) Stage IV late Cu sulfide-bearing veins derived from fluids of a deep mafic intrusion (unexposed) overprint the porphyry system possibly during the Late Devonian or Carboniferous. (c) Early Permian post-collisional shearing and deformation led to stage V argillic alteration. (Color online.)

TABLE 1. Microthermometric data of FIAs from quartz at Yulekenhalasu deposit (Wu 2018)

Alteration stage	Occurrence ^a	Size (μm)	Filling (%)	Type ^b	No. of FIAs	Tm _{H₂O} (°C) ^c			Th-total (°C) ^d			Salinity (wt% NaCl)			Comments
						Min	Max	Mean	Min	Max	Mean	Min	Max	Mean	
Ila potassic alteration	GZ, HF, I	3 to 13	30 to 40	A, B, C	18	-10.3	-1.2	-5.1	288.0	461.0	400.0	2.1	30.0	10.3	
Ilb propylitic alteration	GZ, HF	6	40	A, B	12	-12.7	-1.1	-5.5	164.0	336.0	200.0	1.9	16.6	8.0	
III phyllic alteration	HF, I, S	3 to 9	10 to 30	A, B	10	-8.1	-1.9	-4.1	200.0	387.0	230.0	3.2	11.8	6.5	
IV late Cu sulfide-bearing veins	GZ, HF, S	3 to 12	10 to 60	B, D	32	-6.4	-1.8	-4.6	234.0	317.0	300.0	1.0	17.4	8.5	CO ₂ -bearing
V argillic alteration	HF, S, C	3 to 20	10 to 60	A, B	77	-12.9	-0.2	-4.4	100.0	252.0	160.0	0.4	16.8	6.7	

^a Occurrence: GZ = Growth Zone; HF = Healing Fracture; RD = Randomly Distributed; I = Isolated; S = Scatter; C = Cluster.

^b Type: A = single-phase; B = liquid-vapor two-phase; C = liquid-vapor-solid three phase; D = CO₂-bearing.

^c Tm_{H₂O} = final melting temperature of ice.

^d Th-total = total homogenization temperature.

(2) overprinting by a temporally discrete magmatic-hydrothermal system (e.g., Guo et al. 2011; Masterman et al. 2004, 2005; Nie et al. 2004; Wu et al. 2018); or (3) superimposition of epithermal veins on a preexisting porphyry system (e.g., Cooke and Bloom 1990; Li et al. 2015; Sillitoe 1972). Based on the elemental data of pyrite collected from the Sarekuobu orogenic gold deposit in the Chinese Altay Orogen (Zheng et al. 2021), the estimated median values of Se/S of metamorphic fluids (3×10^{-8}) for orogenic gold deposit in this region is lower than Py_I ($\sim 3 \times 10^{-7}$) and Py_{Ila} ($\sim 1 \times 10^{-6}$; Fig. 9a) from magmatic-hydrothermal fluids. Therefore, the higher Se/S of hydrothermal fluids for stage IV compared to those in orogenic gold systems, combined with the broad overlap of Se/S values for stage IV with magmatic-hydrothermal stages I and IIa pyrite, suggest a magmatic-hydrothermal origin, rather than orogenic (metamorphic) origin (Chen et al. 2007; Goldfarb et al. 2001). During the Late Devonian to Carboniferous, magmatism was widespread in the Chinese Altay–East Junggar (Chen et al. 2001; Han 2008; Wan et al. 2011; Wu et al. 2015, 2019; Zhang et al. 2009). High Ni/Fe in pyrite for stage IV could be explained by an unexposed mafic intrusion source that formed in the island arc during the Late Devonian to Carboniferous at Yulekenhalasu (Fig. 13b), although the possibility of depletion of Fe, which is suggested by the absence of magnetite or hematite (Fig. 3), cannot be excluded. Having excluded the metamorphic and granitic origins for stage IV using pyrite compositions, combined with the fact that mafic magmas formed in island arc settings are characterized by higher CO₂ contents (1246 mm³/g) than those formed in other settings (Tang et al. 2017), the occurrence of CO₂-bearing fluid inclusions in late Cu sulfide-bearing veins suggests that the mafic magma is the most likely origin based on current research. Meanwhile, it is unlikely that stage IV formed by the superimposition of epithermal fluids because of the CO₂-rich characteristics of the fluid inclusions, which imply deeper levels of formation than for the epithermal environment (Chen 2010; Cooke and Simmons 2000; Hedenquist et al. 1998).

The presence of pervasive argillic alteration (stage V) in the post-mineralization alkali granite porphyry (ca. 330 Ma) and continuous stringers of CL-dark quartz cutting across all the earlier quartz generations at Yulekenhalasu are indicators of a younger hydrothermal event (<330 Ma) that produced argillic alteration (Wu 2018). More importantly, the author performed ⁴⁰Ar–³⁹Ar dating of sericite from the argillic alteration (stage V), yielding the weighted plateau age of 277.3 ± 1.3 Ma with two standard deviations (2σ; Online Materials¹ OM1 and OM5). Moreover, Yang et al. (2013) performed ⁴⁰Ar–³⁹Ar dating on muscovite and biotite from the regional shear zone at Yulekenhalasu, yielding plateau ages of 283.8

± 1.5 Ma and 277 ± 2 Ma, respectively, which are interpreted to constrain the deformation age. These ages are roughly coeval with regional deformation associated with the Erqis Fault at 297–261 Ma (Laurent-Charvet et al. 2003). A large number of orogenic Au deposits are distributed along second-order ductile fault zones within 5–10 km of the crustal-scale Erqis fault belt (Pirajno 2013; Wan et al. 2011; Yang et al. 2018a), with their mineralization ages synchronous with the main time of movement of the Erqis Fault during 297–261 Ma, e.g., 292.9 ± 1 Ma for Duolanasayi and 289.2 ± 3.1 Ma for Saidu (Yang et al. 2018a). It is widely accepted that metamorphism caused by deformation generates ore-forming fluids, which extract Au from the wall rocks and migrate upward along the Erqis fault belt as conduits (Chen et al. 2001; Goldfarb et al. 2001; Sibson 2004; Zheng et al. 2021). Gold is then deposited at the brittle-ductile boundary as a result of an acute change of pressure and oxygen fugacity (Cox 2005; Sibson 2004; Zheng et al. 2021). At Yulekenhalasu, stage V argillic alteration was structurally controlled by shear zones and fractures (Figs. 2b, 5d, and 12a). The mineral assemblages in the argillic alteration zone are featured by fine-grained quartz, kaolinite, muscovite, illite, calcite, and pyrite (Fig. 3), which is similar to those in orogenic Au deposits, e.g., carbonates, quartz, muscovite, albite, pyrite, etc. (Chen et al. 2007; Goldfarb et al. 2001). Note that kaolinite has also been reported in orogenic Au deposits in the Chinese Altay and East Junggar region (Feng 2019), with its formation mechanism explained by the reaction of laumontite + CO₂ = kaolinite + calcite + quartz + H₂O (Bucher and Grapes 2011; Wang et al. 2019). Gold inclusions are present in stage V pyrite grains (Fig. 12c), and the highest Au concentrations among all hydrothermal alteration stages were detected in Py_V (Fig. 6c), implying that argillic alteration at Yulekenhalasu could be genetically linked to orogenic Au mineralization in the Chinese Altay–East Junggar region during the Early Permian (Fig. 13c). Besides, it is conceivable to observe superimposition of fluids derived from the Permian orogenic Au mineralization on the Devonian porphyry Cu deposit, given the post-mineralization burial at Yulekenhalasu in the Carboniferous (Wang and Xu 2006).

IMPLICATIONS

Four porphyry-type alteration stages and two stages of overprinting alteration have been identified at Yulekenhalasu, with porphyry-stage potassic and a superimposed late-stage Cu sulfide-bearing vein event being the principal ore-forming stages. Se/S and Co/Ni in pyrite increased with increasing Se/S and Co/Ni in the mineralizing hydrothermal fluids but decreased with increasing temperatures. A Devonian diorite porphyry was the source of porphyry-style alteration and mineralization during stages I–III.

Stage IV late Cu sulfide-bearing veins overprinted the porphyry system in the Late Devonian-Carboniferous, possibly related to an unexposed mafic intrusion. Argillic alteration was produced during regional orogenic Au mineralization and strike-slip deformation in the Early Permian. Consequently, ancient porphyry deposits formed in the Central Asian Orogenic Belt can be modified by post-mineralization events and can cause hypogene upgrading and overprinting of barren alteration assemblages. These can create challenges for mineral exploration but also opportunities for the formation of hybrid hypogene resources such as at Yulekenhalasu. This study indicates that more attention should be paid to the paragenesis study on porphyry Cu deposits in the world's ancient orogenic belts, where various forms of mineralization develop in the same ore district. Moreover, our study highlights using the compositions of pyrite, a widespread mineral in various hydrothermal deposits, as a potential vectoring tool in various magmatic-hydrothermal systems, e.g., porphyry Cu deposit, epithermal deposit, orogenic Au deposit, and polymetallic vein deposit.

ACKNOWLEDGMENTS AND FUNDING

We sincerely thank Zhenjiang Liu from the No. 4 Brigade of the Xinjiang Geology, Mineral Exploration and Development Bureau for field support in the Halasu belt. We also thank Sarah Gilbert and Ivan Belousov for their assistance with laboratory work and sample analysis at the ARC Research Hub for Transforming the Mining Value Chain, CODES, University of Tasmania, Australia. This study was financially supported by the National Key R&D Program of China (2022YFC2903301), National Natural Science Foundation of China (41921003, 41902089, 42230810), Science and Technology Planning of Guangdong Province, China (2020B1212060055) received by Huayong Chen and Chao Wu. This study is also supported by the Guang Dong Major Project of Basic and Applied Basic Research (2019B030302013). This is contribution No. IS-3363 from GIGCAS.

REFERENCES CITED

- Abraitis, P.K., Patrick, R.A.D., and Vaughan, D.J. (2004) Variations in the compositional, textural and electrical properties of natural pyrite: A review. *International Journal of Mineral Processing*, 74, 41–59, <https://doi.org/10.1016/j.minpro.2003.09.002>.
- Acosta-Góngora, P., Gleeson, S.A., Samson, I.M., Ootes, L., and Corriveau, L. (2014) Trace element geochemistry of magnetite and its relationship to Cu-Bi-Co-Au-Ag-U-W mineralization in the Great Bear magmatic zone, NWT, Canada. *Economic Geology and the Bulletin of the Society of Economic Geologists*, 109, 1901–1928, <https://doi.org/10.2113/econgeo.109.7.1901>.
- (2015) Gold refining by bismuth melts in the iron oxide-dominated NICO Au-Co-Bi (±Cu±W) Deposit, NWT, Canada. *Economic Geology and the Bulletin of the Society of Economic Geologists*, 110, 291–314, <https://doi.org/10.2113/econgeo.110.2.291>.
- Acosta-Góngora, P., Potter, E.G., Lawley, C.J.M., Petts, D., and Sparkes, G. (2022) Uraninite chemistry of the Central Mineral Belt, Labrador, Canada: Application of grain-scale unsupervised machine-learning. *Journal of Geochemical Exploration*, 233, 106910, <https://doi.org/10.1016/j.gexplo.2021.106910>.
- Arancibia, O.N. and Clark, A.H. (1996) Early magnetite-amphibole-plagioclase alteration-mineralization in the Island Copper porphyry copper-gold-molybdenum deposit, British Columbia. *Economic Geology and the Bulletin of the Society of Economic Geologists*, 91, 402–438, <https://doi.org/10.2113/gsecongeo.91.2.402>.
- Bajwah, Z.U., Seccombe, P.K., and Offler, R. (1987) Trace element distribution, Co:Ni ratios and genesis of the Big Cadia iron-copper deposit, New South Wales, Australia. *Mineralium Deposita*, 22, 292–300, <https://doi.org/10.1007/BF00204522>.
- Botinelly, T., Siems, D.F., and Sanzolone, R.F. (1985) Trace elements in disseminated sulfides, magnetite, and massive sulfides, West Shasta District, California. *Economic Geology and the Bulletin of the Society of Economic Geologists*, 80, 2196–2205, <https://doi.org/10.2113/gsecongeo.80.8.2196>.
- Bralia, A., Sabatini, G., and Troja, F. (1979) A reevaluation of the Co/Ni ratio in pyrite as geochemical tool in ore genesis problems. *Mineralium Deposita*, 14, 353–374, <https://doi.org/10.1007/BF00206365>.
- Bucher, K. and Grapes, R.H. (2011) *Petrogenesis of Metamorphic Rocks*, 428 p. Springer, <https://doi.org/10.1007/978-3-540-74169-5>.
- Caims, C.P., Mapleson, D.B., Bewsher, A.W., and McCuaig, T.C. (2003) Understanding the structural controls on arsenic mineralisation and ore distribution at the Miitil nickel mine, Widgeemooltha, Western Australia. *Fifth International Mining Geology Conference*, p. 61–72, Bendigo, Victoria.
- Campbell, F.A. and Ethier, V.G. (1984) Nickel and cobalt in pyrrhotite and pyrite from the Faro and Sullivan orebodies. *Canadian Mineralogist*, 22, 503–506.
- Carroll, A.R., Liang, Y., Graham, S.A., Xiao, X.C., Hendrix, M.S., Chu, J.C., and McKnight, C.L. (1990) Junggar basin, northwest China: Trapped Late Paleozoic ocean. *Tectonophysics*, 181, 1–14.
- Chen, Y.J. (2010) On epizonogenism and genetic classification of hydrothermal deposits. *Earth Science Frontiers*, 17, 27–34.
- Chen, H.Y., Chen, Y.J., and Liu, Y.L. (2001) Metallogenesis of the Ertix gold belt, Xinjiang and its relationship to Central Asia-type orogenesis. *Science in China Series D, Earth Sciences*, 44, 245–255, <https://doi.org/10.1007/BF02882259>.
- Chen, Y.J., Ni, P., Fan, H.R., Pirajno, F., Lai, Y., Wenchao, S. and Zhang, H. (2007) Diagnostic fluid inclusions of different types hydrothermal gold deposits. *Yanshi Xuebao*, 23, 2085–2108.
- Cook, N.J., Ciobanu, C.L., and Mao, J. (2009) Textural control on gold distribution in As-free pyrite from the Dongping, Huangtuliang and Hougou gold deposits, North China Craton (Hebei Province, China). *Chemical Geology*, 264, 101–121, <https://doi.org/10.1016/j.chemgeo.2009.02.020>.
- Cooke, D.R. and Bloom, M.S. (1990) Epithermal and subjacent porphyry mineralization, Acupan, Baguio district, Philippines: A fluid-inclusion and paragenetic study. *Journal of Geochemical Exploration*, 35, 297–340, [https://doi.org/10.1016/0375-6742\(90\)90042-9](https://doi.org/10.1016/0375-6742(90)90042-9).
- Cooke, D.R. and Simmons, S.F. (2000) Characteristics and genesis of epithermal gold deposits. *Reviews in Economic Geology*, 13, 221–244.
- Cooke, D.R., Baker, M., Hollings, P., Sweet, G., Chang, Z., Danyushevsky, L., Gilbert, S., Zhou, T., White, N.C., and Gemmel, J.B. (2014) New advances in detecting the distal geochemical footprints of porphyry systems—epidote mineral chemistry as a tool for vectoring and fertility assessments. In K.D. Kelley and H.C. Golden, Eds., *Building Exploration Capability for the 21st Century*, 18, 1–27. Society of Economic Geologists Special Publication.
- Cox, S.F. (2005) Coupling between deformation, fluid pressures, and fluid flow in ore-producing hydrothermal systems at depth in the crust. In J.W. Hedenquist, J.F.H. Thompson, R.J. Goldfarb, and J.P. Richards, Eds., *One Hundredth Anniversary Volume. Society of Economic Geologists*.
- Danyushevsky, L., Robinson, P., Gilbert, S., Norman, M., Large, R., McGoldrick, P., and Shelley, M. (2011) Routine quantitative multi-element analysis of sulphide minerals by laser ablation ICP-MS: Standard development and consideration of matrix effects. *Geochemistry Exploration Environment Analysis*, 11, 51–60, <https://doi.org/10.1144/1467-7873/09-244>.
- Diener, A., Neumann, T., Kramar, U., and Schild, D. (2012) Structure of selenium incorporated in pyrite and mackinawite as determined by XAFS analyses. *Journal of Contaminant Hydrology*, 133, 30–39, <https://doi.org/10.1016/j.jconhyd.2012.03.003>. PubMed
- Du, S.J., Qu, X., Zhang, Y., Cheng, S.L., Lu, H., Wu, Q., and Xu, X. (2010) Chronology and tectonic setting of the intrusive bodies and associated porphyry copper deposit in Hesai area, eastern Junggar. *Yanshi Xuebao*, 26, 2981–2996.
- D'yachkova, I.B. and Khodakovskiy, I.L. (1968) Thermodynamic equilibria in the systems S-H₂O, Se-H₂O, and Te-H₂O in the 25–300 °C temperature range and their geochemical interpretations. *Geochemistry International*, 5, 1108–1125.
- Feng, B. (2019) Remote sensing interpretation of ore-controlling structure of gold deposits in the eastern Junggar metallogenic belt, Xinjiang: Taking the Aermantai-Zhaheba area as an example. Master thesis, China University of Geosciences (Beijing).
- Geng, X.X., Yang, F.Q., Zhang, Z.X., Liu, F., Chai, F.M., and Gao, G.J. (2013) Ore-forming fluid of Yulekenhalasu Cu-Mo deposit on the northern margin of Junggar basin, Xinjiang. *Dizhi Lumping*, 59, 235–247.
- Goldfarb, R.J., Groves, D.I., and Gardoll, S. (2001) Orogenic gold and geologic time: A global synthesis. *Ore Geology Reviews*, 18, 1–75, [https://doi.org/10.1016/S0169-1368\(01\)00016-6](https://doi.org/10.1016/S0169-1368(01)00016-6).
- Guo, W.M., Lu, J.J., Zhang, R.Q., Zhao, Z.J., and Xu, Z.W. (2011) The superimposed mineralization of the Dongguashan Cu deposit in Tongling area, Anhui Province: Evidence from the ore texture. *Acta Geologica Sinica*, 85, 1223–1232.
- Han, B.F. (2008) A preliminary comparison of Mesozoic granitoids and rare metal deposits in Chinese and Russian Altai Mountains. *Yanshi Xuebao*, 24, 655–660.
- Han, B.F., Ji, J.Q., Song, B., Chen, L.H., and Li, Z.H. (2004) SHRIMP zircon U-Pb ages of Kalatongke No. 1 and Huangshandong Cu-Ni-bearing mafic-ultramafic complexes, north Xinjiang, and geological implications. *Chinese Science Bulletin*, 49, 2424–2429.
- Hawley, J.E. and Nichol, I. (1959) Selenium in some Canadian sulfides. *Economic Geology and the Bulletin of the Society of Economic Geologists*, 54, 608–628, <https://doi.org/10.2113/gsecongeo.54.4.608>.
- Hedenquist, J.W., Arribas, A., and Reynolds, T.J. (1998) Evolution of an intrusion-centered hydrothermal system: Far Southeast-Lepanto porphyry and epithermal Cu-Au deposits, Philippines. *Economic Geology and the Bulletin of the Society of Economic Geologists*, 93, 373–404, <https://doi.org/10.2113/gsecongeo.93.4.373>.
- Heinhorst, J., Lehmann, B., Ermolov, P., Serykh, V., and Zhurutin, S. (2000) Paleozoic crustal growth and metallogeny of Central Asia: Evidence from magmatic-hydrothermal ore systems of Central Kazakhstan. *Tectonophysics*, 328, 69–87, [https://doi.org/10.1016/S0040-1951\(00\)00178-5](https://doi.org/10.1016/S0040-1951(00)00178-5).
- Hong, T., Klemd, R., Gao, J., Xiang, P., Xu, X.W., You, J., Wang, X.S., Wu, C., Li, H., and Ke, Q. (2017) The tectonic evolution of the Irtysh tectonic belt: New zircon U-Pb ages of arc-related and collisional granitoids in the Kalaxiangar tectonic belt, NW China. *Lithos*, 272–273, 46–68, <https://doi.org/10.1016/j.lithos.2016.12.001>.

- Hong, T., Xu, X.-W., Gao, J., Peters, S.G., Li, J., Cao, M., Xiang, P., Wu, C., and You, J. (2018) Element migration of pyrites during ductile deformation of the Yuleken porphyry Cu deposit (NW-China). *Ore Geology Reviews*, 100, 205–219, <https://doi.org/10.1016/j.oregeorev.2017.10.019>.
- Hong, T., Dolejs, D., Zhai, M.G., Oscar, L., Xu, X.W., Gao, J., Schloglova, K.D., and Wang, Y.J. (2021a) Multiple tectonic-magmatic Mo-enrichment events in Yuleken porphyry Cu-Mo deposit, NW China and its' implications for the formation of giant porphyry Mo deposit. *Ore Geology Reviews*, 139, 104401, <https://doi.org/10.1016/j.oregeorev.2021.104401>.
- Hong, T., Hollings, P., Zhai, M.-G., Wang, Y.-X., Xu, X.-W., Gao, J., and Wang, Y.-J. (2021b) Superimposed mineralization in the deformed Yulekenhalasu porphyry Cu-Mo deposit (Northwest China): Rb-Sr geochronology, S isotope, and trace element analysis of chalcopyrite. *Ore Geology Reviews*, 135, 104226, <https://doi.org/10.1016/j.oregeorev.2021.104226>.
- Huston, D.L., Sie, S.H., Suter, G.F., Cooke, D.R., and Both, R.A. (1995) Trace elements in sulfide minerals from eastern Australian volcanic-hosted massive sulfide deposits; Part I, Proton microprobe analyses of pyrite, chalcopyrite, and sphalerite, and Part II, Selenium levels in pyrite; comparison with delta ³⁴S values and implications for the source of sulfur in volcanogenic hydrothermal systems. *Economic Geology and the Bulletin of the Society of Economic Geologists*, 90, 1167–1196, <https://doi.org/10.2113/gsecongeo.90.5.1167>.
- Jahn, B.M. (2004) The Central Asian Orogenic Belt and growth of the continental crust in the Phanerozoic. Special Publication Geological Society of London, 226, 73–100, <https://doi.org/10.1144/GSL.SP.2004.226.01.05>.
- Jahn, B.M., Wu, F.Y., and Chen, B. (2000) Granitoids of the Central Asian Orogenic Belt and continental growth in the Phanerozoic. *Earth and Environmental Science Transactions of the Royal Society of Edinburgh*, 91, 181–193.
- Keith, M., Hackel, F., Haase, K.M., Schwarz-Schampera, U., and Klemm, R. (2016) Trace element systematics of pyrite from submarine hydrothermal vents. *Ore Geology Reviews*, 72, 728–745, <https://doi.org/10.1016/j.oregeorev.2015.07.012>.
- Keith, M., Smith, D.J., Jenkin, G.R.T., Holwell, D.A., and Dye, M.D. (2018) A review of Te and Se systematics in hydrothermal pyrite from precious metal deposits: Insights into ore-forming processes. *Ore Geology Reviews*, 96, 269–282, <https://doi.org/10.1016/j.oregeorev.2017.07.023>.
- Large, R.R., Danyushevsky, L., Hollit, C., Maslennikov, V., Meffre, S., Gilbert, S., Bull, S., Scott, R., Emso, P., Thomas, H., and others. (2009) Gold and trace element zonation in pyrite using a laser imaging technique: Implications for the timing of gold in orogenic and Carlin-style sediment-hosted deposits. *Economic Geology and the Bulletin of the Society of Economic Geologists*, 104, 635–668, <https://doi.org/10.2113/gsecongeo.104.5.635>.
- Large, R., Bull, S.W., and Maslennikov, V.V. (2011) A Carbonaceous sedimentary source-rock model for Carlin-type and orogenic gold deposits. *Economic Geology and the Bulletin of the Society of Economic Geologists*, 106, 331–358, <https://doi.org/10.2113/gsecongeo.106.3.331>.
- Large, R.R., Halpin, J.A., Danyushevsky, L.V., Maslennikov, V.V., Bull, S.W., Long, J.A., Gregory, D.D., Lounejeva, E., Lyons, T.W., Sack, P.J., and others. (2014) Trace element content of sedimentary pyrite as a new proxy for deep-time ocean-atmosphere evolution. *Earth and Planetary Science Letters*, 389, 209–220, <https://doi.org/10.1016/j.epsl.2013.12.020>.
- Laurent-Charvet, S., Charvet, J., Monié, P., and Shu, L. (2003) Late Paleozoic strike-slip shear zones in eastern Central Asia (NW China): New structural and geochronological data. *Tectonics*, 22, 1009, <https://doi.org/10.1029/2001TC901047>.
- Layton-Matthews, D., Peter, J.M., Scott, S.D., and Leybourne, M.I. (2008) Distribution, mineralogy, and geochemistry of selenium in felsic volcanic-hosted massive sulfide deposits of the Finlayson Lake district, Yukon Territory, Canada. *Economic Geology and the Bulletin of the Society of Economic Geologists*, 103, 61–88, <https://doi.org/10.2113/gsecongeo.103.1.61>.
- Li, W.B., Zhong, R.C., Xu, C., Song, B., and Qu, W.J. (2012) U-Pb and Re-Os geochronology of the Bainaimiao Cu-Mo-Au deposit, on the northern margin of the North China Craton, Central Asia Orogenic Belt: Implications for ore genesis and geodynamic setting. *Ore Geology Reviews*, 48, 139–150, <https://doi.org/10.1016/j.oregeorev.2012.03.001>.
- Li, Q., Zhang, Z.X., Geng, X.X., Li, C., Liu, F., Chai, F.M., and Yang, F.Q. (2014) Geology and geochemistry of the Qiaoxiahala Fe-Cu-Au deposit, Junggar region, northwest China. *Ore Geology Reviews*, 57, 462–481, <https://doi.org/10.1016/j.oregeorev.2013.08.003>.
- Li, G.M., Zhang, X.N., Qin, K.Z., Sun, X.G., Zhao, J.X., Yin, X.B., Li, J.X., and Yuan, H.S. (2015) The telescoped porphyry-high sulfidation epithermal Cu-(Au) mineralization of Rongna deposit in Duolong ore cluster at the southern margin of Qiangtang Terrane, Central Tibet: Integrated evidence from geology, hydrothermal alteration and sulfide assemblages. *Yanshi Xuebao*, 31, 2307–2324.
- Liu, T.G., Yu, X.Y., and Mei, H.J. (1991) The Duolanasayi-Kalaxiang'er porphyry copper-gold metallogenic belt. *Geology and Geochemistry*, 2, 71–74.
- Liu, G.R., Dong, L.H., Xue, C.J., Li, X.R., Zhang, L.W., Wei, G.Z., He, L.X., Zhao, Z.H., Qin, J.H., and Zhang, Z.X. (2010) Geological characteristics and exploration direction of the Yulekenhalasu copper deposit. *Xinjiang Geology*, 28, 377–384.
- Liu, W., Migdisov, A., and Williams-Jones, A. (2012) The stability of aqueous nickel (II) chloride complexes in hydrothermal solutions: Results of UV-Visible spectroscopic experiments. *Geochimica et Cosmochimica Acta*, 94, 276–290, <https://doi.org/10.1016/j.gca.2012.04.055>.
- Loftus-Hills, G. and Solomon, M. (1967) Cobalt, nickel and selenium in sulphides as indicators of ore genesis. *Mineralium Deposita*, 2, 228–242, <https://doi.org/10.1007/BF00201918>.
- Long, L.L., Wang, Y.W., Du, A.D., Wang, J.B., Wang, L.J., Wang, S.L., Pu, K.X., and Qu, W.J. (2011) Molybdenite Re-Os age of Xilekuduke Cu-Mo deposit in Xinjiang and its geological significance. *Mineralium Deposita*, 30, 635–644.
- Lorand, J.-P., Alard, O., Luguët, A., and Keays, R.R. (2003) Sulfur and selenium systematics of the subcontinental lithospheric mantle: Inferences from the Massif Central xenolith suite (France). *Geochimica et Cosmochimica Acta*, 67, 4137–4151, [https://doi.org/10.1016/S0016-7037\(03\)00305-3](https://doi.org/10.1016/S0016-7037(03)00305-3).
- Loucks, R.R. (2014) Distinctive composition of copper-ore-forming arc magmas. *Journal of the Geological Society of Australia*, 61, 5–16.
- Mao, J.W., Pirajno, F., Lehmann, B., Luo, M.C., and Berzina, A. (2014) Distribution of porphyry deposits in the Eurasian continent and their corresponding tectonic settings. *Journal of Asian Earth Sciences*, 79, 576–584, <https://doi.org/10.1016/j.jseas.2013.09.002>.
- Masterman, G.J., Cooke, D.R., Berry, R.F., Clark, A.H., Archibald, D.A., Mathur, R., Walshe, J.L., and Duran, M. (2004) ⁴⁰Ar/³⁹Ar and Re-Os geochronology of porphyry copper-molybdenum deposits and related copper-silver veins in the Collahuasi District, northern Chile. *Economic Geology and the Bulletin of the Society of Economic Geologists*, 99, 673–690, <https://doi.org/10.2113/gsecongeo.99.4.673>.
- Masterman, G.J., Cooke, D.R., Berry, R.F., Walshe, J.L., Lee, A.W., and Clark, A.H. (2005) Fluid chemistry, structural setting, and emplacement history of the Rosario Cu-Mo porphyry and Cu-Ag-Au epithermal veins, Collahuasi district, northern Chile. *Economic Geology and the Bulletin of the Society of Economic Geologists*, 100, 835–862, <https://doi.org/10.2113/gsecongeo.100.5.835>.
- Melekestseva, I.Y., Tret'yakov, G.A., Nimis, P., Yuminov, A.M., Maslennikov, V.V., Maslennikova, S.P., Kotlyarov, V.A., Beltenev, V.E., Danyushevsky, L.V., and Large, R. (2014) Barite-rich massive sulfides from the Semenov-1 hydrothermal field (Mid-Atlantic Ridge, 13°30'87" N): Evidence for phase separation and magmatic input. *Marine Geology*, 349, 37–54, <https://doi.org/10.1016/j.margeo.2013.12.013>.
- Mossakovsky, A.A., Ruzhentsev, S.V., Samygin, S.G., and Kheraskova, T.N. (1994) Central Asian fold belt: Geodynamic evolution and formation history. *Geotectonics*, 27, 445–474.
- Nie, F.J., Jiang, S.H., Zhang, Y., Liu, Y., and Hu, P. (2004) Geological features and origin of porphyry copper deposits in China-Mongolia border region and its neighboring areas. *Journal of Asian Earth Sciences*, 23, 176–189.
- Niu, L., Hong, T., Xu, X.W., Li, H., Ke, Q., Wang, X.H., and Ma, Y.C. (2020) A revised stratigraphic and tectonic framework for the Ashele volcanogenic massive sulfide deposit in the southern Chinese Altay: Evidence from stratigraphic relationships and zircon geochronology. *Ore Geology Reviews*, 127, 103814, <https://doi.org/10.1016/j.oregeorev.2020.103814>.
- Perelló, J., Cox, D., Garamjav, D., Sanjdorj, S., Diakov, S., Schissel, D., Munkhbat, T.-O., and Oyun, G. (2001) Oyu Tolgoi, Mongolia: Siluro-Devonian porphyry Cu-Au-(Mo) and high-sulfidation Cu mineralization with a Cretaceous chalcocite blanket. *Economic Geology and the Bulletin of the Society of Economic Geologists*, 96, 1407–1428, <https://doi.org/10.2113/gsecongeo.96.6.1407>.
- Pirajno, F. (2013) *The Geology and Tectonic Settings of China's Mineral Deposits*, p. 909–910. Springer.
- Qin, K.Z., Zhang, L.C., Ding, K.S., Xu, Y.X., Tang, D.M., Xu, X.W., Ma, T.L., and Li, G.M. (2009) Mineralization type, Petrogenesis of ore-bearing intrusions and mineralogical characteristics of Sanchakou copper deposits in eastern Tianshan. *Yanshi Xuebao*, 25, 845–861.
- Reich, M., Deditius, A., Chrysosoulis, S., Li, J.W., Ma, C.Q., Parada, M.A., Barra, F., and Mittermayr, F. (2013) Pyrite as a record of hydrothermal fluid evolution in a porphyry copper system: A SIMS/EMPA trace element study. *Geochimica et Cosmochimica Acta*, 104, 42–62, <https://doi.org/10.1016/j.gca.2012.11.006>.
- Seltmann, R., Porter, T.M., and Pirajno, F. (2014) Geodynamics and metallogeny of the central Eurasian porphyry and related epithermal mineral systems: A review. *Journal of Asian Earth Sciences*, 79, 810–841, <https://doi.org/10.1016/j.jseas.2013.03.030>.
- Şengör, A.M.C., Natal'in, B.A., and Burtman, V.S. (1993) Evolution of the Altaid tectonic collage and Palaeozoic crustal growth in Eurasia. *Nature*, 364, 299–307, <https://doi.org/10.1038/364299a0>.
- Sibson, R.H. (2004) Controls on maximum fluid overpressure defining conditions for mesozonal mineralisation. *Journal of Structural Geology*, 26, 1127–1136, <https://doi.org/10.1016/j.jsg.2003.11.003>.
- Sillitoe, R.H. (1972) A plate tectonic model for the origin of porphyry copper deposits. *Economic Geology and the Bulletin of the Society of Economic Geologists*, 67, 184–197, <https://doi.org/10.2113/gsecongeo.67.2.184>.
- (2010) Porphyry copper systems. *Economic Geology and the Bulletin of the Society of Economic Geologists*, 105, 3–41, <https://doi.org/10.2113/gsecongeo.105.1.3>.
- Sykora, S., Cooke, D.R., Meffre, S., Stephanov, A.S., Gardner, K., Scott, R., Selley, D., and Harris, A.C. (2018) Evolution of pyrite trace element compositions from porphyry-style and epithermal conditions at the Lihir gold deposit: Implications for ore genesis and mineral processing. *Economic Geology and the Bulletin of the Society of Economic Geologists*, 113, 193–208, <https://doi.org/10.5382/econgeo.2018.4548>.
- Tang, Q., Zhang, M., Feng, P., Wang, Y., Sun, F., Dang, Y., Wang, X., and Hu, F. (2017) The chemical compositions and environmental implications of Carbonaceous

- volatile species of the mafic magmatism in different tectonic settings. *Bulletin of Mineralogy Petrology and Geochemistry*, 36, 237–244.
- Tischendorf, G. (1966) Zur verteilung des selens in sulfiden. *Freiberger Forschungshefte*, 208, 1–162.
- Wan, B., Xiao, W.J., Zhang, L.C., Windley, B.F., Han, C.M., and Quinn, C.D. (2011) Contrasting styles of mineralization in the Chinese Altai and East Junggar, NW China: Implications for the accretionary history of the southern Altaids. *Journal of the Geological Society*, 168, 1311–1321, <https://doi.org/10.1144/0016-76492011-021>.
- Wan, B., Xiao, W.J., Han, C.M., Windley, B.F., Zhang, L.C., Qu, W.J., and Du, A.D. (2014) Re-Os molybdenite age of the Cu-Mo skarn ore deposit at Suoerkuduke in East Junggar, NW China and its geological significance. *Ore Geology Reviews*, 56, 541–548, <https://doi.org/10.1016/j.oregeorev.2013.02.011>.
- Wan, B., Xiao, W.J., Windley, B.F., Gao, J., Zhang, L.C., and Cai, K. (2017) Contrasting ore styles and their role in understanding the evolution of the Altaids. *Ore Geology Reviews*, 80, 910–922, <https://doi.org/10.1016/j.oregeorev.2016.08.025>.
- Wang, J.B. and Xu, X. (2006) Post-collisional tectonic evolution and metallogenesis in northern Xinjiang, China. *Acta Geologica Sinica*, 80, 23–31.
- Wang, T., Tong, Y., Li, S., Zhang, J.J., Shi, X.J., Li, J.Y., Han, B.F., and Hong, D.W. (2010) Spatial and temporal variations of granitoids in the Altay orogen and their implications for tectonic setting and crustal growth: Perspectives from Chinese Altay. *Acta Petrologica et Mineralogica*, 29, 595–618.
- Wang, Y.F., Chen, H.Y., Han, J.S., Chen, S.B., Huang, B.Q., Li, C., Tian, Q.L., Wang, C., Wu, J.X., and Chen, M.X. (2018) Paleozoic tectonic evolution of the Dananhu-Tousuquan island arc belt, Eastern Tianshan: Constraints from the magmatism of the Yuhai porphyry Cu deposit, Xinjiang, NW China. *Journal of Asian Earth Sciences*, 153, 282–306, <https://doi.org/10.1016/j.jseaes.2017.05.022>.
- Wang, Y.F., Chen, H.Y., Baker, M.J., Han, J.S., Xiao, B., Yang, J.T., and Jourdan, F. (2019) Multiple mineralization events of the Paleozoic Tuwu porphyry copper deposit, Eastern Tianshan: Evidence from geology, fluid inclusions, sulfur isotopes, and geochronology. *Mineralium Deposita*, 54, 1053–1076, <https://doi.org/10.1007/s00126-018-0859-4>.
- Wang, Y.F., Chen, H.Y., Falloon, T.J., and Han, J.S. (2022) The Paleozoic-Mesozoic magmatic evolution of the Eastern Tianshan, NW China: Constraints from geochronology and geochemistry of the Sanchakou intrusive complex. *Gondwana Research*, 103, 1–22, <https://doi.org/10.1016/j.gr.2021.11.002>.
- Windley, B.F., Kröner, A., Guo, J.H., Qu, G.S., Li, Y.Y., and Zhang, C. (2002) Neoproterozoic to Paleozoic geology of the Altai orogen, NW China: New zircon age data and tectonic evolution. *The Journal of Geology*, 110, 719–737, <https://doi.org/10.1086/342866>.
- Wohlgemuth-Ueberwasser, C.C., Viljoen, F., Petersen, S., and Vorster, C. (2015) Distribution and solubility limits of trace elements in hydrothermal black smoker sulfides: An in-situ LA-ICP-MS study. *Geochimica et Cosmochimica Acta*, 159, 16–41, <https://doi.org/10.1016/j.gca.2015.03.020>.
- Wu, C. (2018) Magmatic evolution and multiphase superimposing mineralization in the Halasu Cu belt, Xinjiang, 186 p. Ph.D. thesis, Guangzhou Institute of Geochemistry, Chinese Academy of Sciences.
- Wu, C., Chen, H.Y., Hollings, P., Xu, D.R., Liang, P., Han, J.S., Xiao, B., Cai, K.D., Liu, Z.J., and Qi, Y.K. (2015) Magmatic sequences in the Halasu Cu Belt, NW China: Trigger for the Paleozoic porphyry Cu mineralization in the Chinese Altay-East Junggar. *Ore Geology Reviews*, 71, 373–404, <https://doi.org/10.1016/j.oregeorev.2015.06.017>.
- Wu, C., Chen, H.Y., Liang, P., Han, J.S., Liu, Z.J., Fang, J., and Xu, D.R. (2018) Paragenesis and fluid evolution of the Halasu III porphyry Cu deposit, East Junggar (NW China): Implications for the Paleozoic multiphase superimposing mineralization in the Central Asian Orogenic Belt. *Ore Geology Reviews*, 100, 183–204, <https://doi.org/10.1016/j.oregeorev.2016.08.001>.
- Wu, C., Chen, H.Y., Hong, W., Li, D.F., Liang, P., Fang, J., Zhang, L.J., and Lai, C. (2019) Magnetite chemistry and implications for the magmatic-hydrothermal ore-forming process: An example from the Devonian Yuleken porphyry Cu system, NW China. *Chemical Geology*, 522, 1–15, <https://doi.org/10.1016/j.chemgeo.2019.04.022>.
- Xiang, P. (2013) Geological characteristics, metallogenic epoch and its evolution process of the superimposed and tectonic reworked porphyry Cu-Mo deposits in the Kalaxiang porphyry copper ore belt, eastern Junggar. 187 p. Ph.D. thesis, Chinese University of Geosciences, Chinese University of Geosciences, Beijing, China.
- Xiang, P., Zhang, L.C., Xu, X.W., Liu, G.R., Liu, Z.J., Jin, X.D., and Li, W.J. (2012) Geological characteristics and genesis of Yuleken-Halasu superimposed and tectonically reworked porphyry copper-gold (molybdenum) deposit in Qinghe, Xinjiang. *Yanshi Xuebao*, 28, 2369–2380.
- Xiao, W.J., Windley, B.F., Huang, B.C., Han, C.M., Yuan, C., Chen, H.L., Sun, M., Sun, S., and Li, J.L. (2009a) End-Permian to mid-Triassic termination of the accretionary processes of the southern Altaids: Implications for the geodynamic evolution, Phanerozoic continental growth, and metallogeny of Central Asia. *International Journal of Earth Sciences*, 98, 1189–1217, <https://doi.org/10.1007/s00531-008-0407-z>.
- Xiao, W.J., Windley, B.F., Yuan, C., Sun, M., Han, C.M., Lin, S.F., Chen, H.L., Yan, Q.R., Liu, D.Y., Qin, K.Z., and others. (2009b) Paleozoic multiple subduction-accretion processes of the southern Altaids. *American Journal of Science*, 309, 221–270, <https://doi.org/10.2475/03.2009.02>.
- Xiao, B., Chen, H.Y., Hollings, P., Han, J.S., Wang, Y.F., Yang, J.T., and Cai, K. (2017) Magmatic evolution of the Tuwu-Yandong porphyry Cu belt, NW China: Constraints from geochronology, geochemistry and Sr-Nd-Hf isotopes. *Gondwana Research*, 43, 74–91, <https://doi.org/10.1016/j.gr.2015.09.003>.
- Xue, C.J., Chi, G.X., Zhao, X.B., Wu, G.G., Zhao, Z.F., and Dong, L.H. (2016) Multiple and prolonged porphyry Cu-Au mineralization and alteration events in the Halasu deposit, Chinese Altai, Xinjiang, northwestern China. *Geoscience Frontiers*, 7, 799–809, <https://doi.org/10.1016/j.gsf.2015.10.008>.
- Yakubchuk, A. (2004) Architecture and mineral deposit settings of the Altai orogenic collage: A revised model. *Journal of Asian Earth Sciences*, 23, 761–779, <https://doi.org/10.1016/j.jseaes.2004.01.006>.
- Yakubchuk, A., Degtyarev, K., Maslennikov, V., Wurst, A., Stekhin, A., and Lobanov, K. (2012) Tectonomagmatic settings, architecture, and metallogeny of the Central Asian copper province. *Society of Economic Geologists Special Publication*, 16, 403–432.
- Yamamoto, M. (1976) Relationship between Se/S and sulfur isotope ratios of hydrothermal sulfide minerals. *Mineralium Deposita*, 11, 197–209, <https://doi.org/10.1007/BF00204481>.
- Yan, S.H., Teng, R.L., Zhang, Z.C., Chen, B.L., Chen, W., Zhou, G., and He, L.X. (2006) New understanding on origin of Kalaxiang copper deposit on southern margin of Altay mountain, Xinjiang: Constraints from S-Pb-H-O isotope geochemistry and ⁴⁰Ar-³⁹Ar age of Halasu copper deposit. *Mineralium Deposita*, 25, 292–301.
- Yang, F.Q., Liu, G.R., Qin, J.H., Zhang, Z.X., Liu, Z.J., Zhang, L.W., Wei, G.Z., Liu, F., and Geng, X.X. (2012) Fluid inclusion and stable isotope study of Yulekenhalasu copper-(molybdenum) deposit in northern margin of Junggar, Xinjiang. *Mineralium Deposita*, 31, 965–982.
- Yang, F.Q., Qin, J.H., Liu, F., Zhang, Z.X., Liu, Z.J., Geng, X.X., Chai, F.M., and Gao, W.J. (2013) Ar-Ar dating of the ductile shear zones in the Yulekenhalasu Cu-(Mo) ore deposit. *Dadi Gouzaoyu Chengkuangxue*, 37, 1–10.
- Yang, F.Q., Chai, F.M., Zhang, Z.X., Geng, X.X., and Li, Q. (2014) Zircon U-Pb geochronology, geochemistry, and Sr-Nd-Hf isotopes of granitoids in the Yulekenhalasu copper ore district, northern Junggar, China: Petrogenesis and tectonic implications. *Lithos*, 190–191, 85–103, <https://doi.org/10.1016/j.lithos.2013.12.003>.
- Yang, F.Q., Geng, X.X., Wang, R., Zhang, Z.X., and Guo, X.J. (2018a) A synthesis of mineralization styles and geodynamic settings of the Paleozoic and Mesozoic metallic ore deposits in the Altay Mountains, NW China. *Journal of Asian Earth Sciences*, 159, 233–258, <https://doi.org/10.1016/j.jseaes.2017.05.020>.
- Yang, F.Q., Li, Q., Yang, C.D., and Zhang, Z.X. (2018b) A combined fluid inclusion and S-H-O-He-Ar isotope study of the Devonian Ashele VMS-type copper-zinc deposit in the Altay orogenic belt, northwest China. *Journal of Asian Earth Sciences*, 161, 139–163, <https://doi.org/10.1016/j.jseaes.2018.05.012>.
- Zhang, Z.C., Zhou, G., Kusky, T.M., Yan, S.H., Chen, B.L., and Zhao, L. (2009) Late Paleozoic volcanic record of the Eastern Junggar terrane, Xinjiang, Northwestern China: Major and trace element characteristics, Sr-Nd isotopic systematics and implications for tectonic evolution. *Gondwana Research*, 16, 201–215, <https://doi.org/10.1016/j.gr.2009.03.004>.
- Zhao, Y.M., Bi, C.S., Zou, X.Q., Sun, Y.L., Du, A.D., and Zhao, Y.M. (1997) The Re-Os isotopic age of molybdenite from Duobaoshan and Tongshan porphyry copper (molybdenite) deposits. *Yanshi Xuebao*, 18, 61–67.
- Zhao, H.-X., Frimmel, H.E., Jiang, S.-Y., and Dai, B.-Z. (2011) LA-ICP-MS trace element analysis of pyrite from the Xiaqingling gold district, China: Implications for ore genesis. *Ore Geology Reviews*, 43, 142–153, <https://doi.org/10.1016/j.oregeorev.2011.07.006>.
- Zheng, Y., Wu, Y.H., Yu, P.P., Hu, Z.B., and Chen, Y.J. (2021) Gold accumulation in the metavolcanic-hosted orogenic gold deposit constrained by pyrite paragenesis coupled with in-situ trace elements and sulfur isotope: The Sarekuobu example in the Chinese Altay Orogen. *Ore Geology Reviews*, 138, 104387, <https://doi.org/10.1016/j.oregeorev.2021.104387>.
- Zhou, T.F., Zhang, L.J., Yuan, F., Fan, Y., and Cooke, D.R. (2010) LA-ICP-MS in situ trace element analysis of pyrite from the Xinqiao Cu-Au-S deposit in Tongling, Anhui, and its constraints on the ore genesis. *Earth Science Frontiers*, 17, 306–319.

MANUSCRIPT RECEIVED JULY 25, 2022

MANUSCRIPT ACCEPTED JUNE 11, 2023

ACCEPTED MANUSCRIPT ONLINE JUNE 21, 2023

MANUSCRIPT HANDLED BY CALLUM HETHERINGTON

Endnote:

¹Deposit item AM-24-58727. Online Materials are free to all readers. Go online, via the table of contents or article view, and find the tab or link for supplemental materials.